

A fast multipole method for stellar dynamics

Walter Dehnen

March 26, 2018

Abstract The approximate computation of all gravitational forces between N interacting particles via the fast multipole method (FMM) can be made as accurate as direct summation, but requires less than $\mathcal{O}(N)$ operations. FMM groups particles into spatially bounded cells and uses cell-cell interactions to approximate the force at *any* position within the sink cell by a Taylor expansion obtained from the multipole expansion of the source cell. By employing a novel estimate for the errors incurred in this process, I minimise the computational effort required for a given accuracy and obtain a well-behaved distribution of force errors. For relative force errors of $\sim 10^{-7}$, the computational costs exhibit an empirical scaling of $\propto N^{0.87}$. My implementation (running on a 16 core node) out-performs a GPU-based direct summation with comparable force errors for $N \gtrsim 10^5$.

Keywords methods: numerical — methods: N -body simulations

1 Introduction

The computation of the mutual gravitational forces at every time step dominates the computational costs of all N -body simulations. When simulating collisionless stellar dynamics, the N -body model is merely a Monte-Carlo representation of a smooth phase-space distribution and the N -body force is only ever an *estimate* for the smooth force field of the continuous system modelled (see also Dehnen and Read, 2011). In particular, the N -body force unavoidably carries an *estimation error*. This motivates the use of *approximate* methods for computing the N -body force, such as the Barnes and Hut (1986) tree code, as long as the approximation errors are small compared to the estimation errors.

N -body simulations of collisional stellar dynamics are of a completely different nature. Here, the particles simulate individual stars and the N -body force carries no estimation error. Consequently, the (negative) gravitational potential

$$\Psi(\mathbf{x}_b) = \sum_{a \neq b} G\mu_a \psi(\mathbf{x}_b - \mathbf{x}_a) \quad \text{with} \quad \psi(\mathbf{r}) = |\mathbf{r}|^{-1} \quad (1)$$

and its derivative, the acceleration, must be calculated with high accuracy. This is typically achieved by *direct summation*, when equation (1) is translated into computer code and the only errors are owed to finite computational precision.

This computation incurs a cost of $\mathcal{O}(N)$ for a single particle and thus $\mathcal{O}(N^2)$ per unit time for running a full simulation. As a consequence, realistic simulations with $N \sim 10^6$ for globular clusters and galactic centres are still very challenging and large parameter studies impossible. Measures employed to ameliorate this situation include the usage of powerful special-purpose hardware devices (Makino and Taiji, 1998) or graphical processing units (GPUs, Gaburov et al, 2009), as well as separating the highly fluctuating forces due to close neighbours, in order to reduce the frequency of expensive far-field force computations (Ahmad and Cohen, 1973).

While these measures substantially reduce the effective costs, the complexity of N^2 remains. The alternative of using approximate methods also for collisional stellar dynamics is so far untested. The requirements for such a method differ from that in collisionless N -body methods in two important aspects: (i) there is no gravitational softening and (ii) to preserve the validity of the N -body model, the approximation errors must be much smaller than what is common in collisionless N -body simulations.

A straightforward approach is to use the tree code with a small opening angle and/or high expansion order, resulting in a scheme with $\mathcal{O}(N \ln N)$ costs. A more efficient approach is to use the *fast multipole method* (FMM; Greengard and Rokhlin, 1987; Cheng, Greengard, and Rokhlin,

1999), which has costs of only $\mathcal{O}(N)$. An initial attempt by Capuzzo-Dolcetta and Mocchi (1998) to port this technique from its original realm of molecular dynamics to astrophysics failed to obtain better practical efficiency than the tree code. However, when adapting the FMM to the inhomogeneity of stellar systems and the low force accuracy required in collisionless dynamics (by using a hierarchical tree data structure and a flexible opening angle), it is substantially faster than the tree code (Dehnen, 2000, 2002).

The critical question here is whether FMM can be tuned to be more efficient than direct summation at force accuracies and particle numbers required by collisional N -body techniques. The goal of this study is to address this question by tuning FMM for the application to collisional N -body simulations, investigating the resulting dependence of computational costs and numerical accuracy on the various numerical parameters, and assessing its practical efficiency.

This paper is organised as follows. In Section 2 and Appendix A, the mathematical (and algorithmic) foundations of FMM are derived and laid down. Section 3 (and Appendix B) introduces and motivates my approach for quantifying the resulting acceleration errors; Section 4 provides useful estimates for the errors of individual FMM interactions; Section 5 deals with optimising the multipole-acceptance criterion; and in Section 6 the method is tuned to obtain a force accuracy target with minimal computational effort. Finally, in Section 7 possible extensions and applications are discussed, and Section 8 concludes.

2 FMM basics

The tree code approximates the sum (1) by first dividing source particles a into groups bounded by geometric cells, each of which is well-separated from the sink position \mathbf{x}_b , and then computing the forces of each source cell from their multipole moments. This corresponds to Taylor expanding the Greens function $\psi(\mathbf{x}_b - \mathbf{x}_a)$ about the distance to an appropriate centre \mathbf{z} of each source cell.

The essence of the fast multipole method is to Taylor expand the Greens function not only at the source positions \mathbf{x}_a , but also at the sink positions \mathbf{x}_b . This latter amounts to approximating (a contribution to) the gravitational field within each sink cell by its local Taylor expansion about some appropriate potential expansion centre \mathbf{s} . Obviously, this approach is beneficial only if the forces for a large fraction of the sinks within a cell are to be computed simultaneously.

2.1 Mathematical background

The FMM relations are most easily derived using Cartesian coordinates. However, for Newtonian gravity, $\psi = |\mathbf{r}|^{-1}$, the resulting relations are inefficient. Instead, exploiting that this

Greens function satisfies $\nabla^2 \psi = 0$ for $\mathbf{r} \neq 0$ naturally leads to spherical harmonics. Cheng et al (1999) have already given (without derivation) the corresponding FMM relations, but in a form ill-suited for computer code. In Appendix A, I derive equivalent but much more compact and computationally convenient relations. These are summarised here.

Let $\mathbf{r} = (x, y, z)$ with spherical polar coordinates r, θ, ϕ , then

$$\Theta_n^m(\mathbf{r}) = (-1)^m \frac{(n-m)!}{r^{n+1}} P_n^m(\cos \theta) e^{im\phi}, \quad (2a)$$

$$\Upsilon_n^m(\mathbf{r}) = (-1)^m \frac{r^n}{(n+m)!} P_n^m(\cos \theta) e^{im\phi} \quad (2b)$$

with integer indices $0 \leq |m| \leq n$ are (complex-valued) harmonic functions, i.e. $\nabla^2 \Upsilon_n^m = 0$ for all \mathbf{r} and $\nabla^2 \Theta_n^m = 0$ for all $\mathbf{r} \neq 0$. The Υ_n^m are homogeneous polynomials of total degree n in x, y , and z (they are defined in Appendix A.3 without reference to polar coordinates; see also Table 3). With these definitions, the FMM relations for the computation of the potential due to all particles within source cell A and at any position \mathbf{x}_b within sink cell B are

$$\Psi_{A \rightarrow B}(\mathbf{x}_b) = \sum_{n=0}^p \sum_{m=-n}^n \Upsilon_n^{m*}(\mathbf{s}_B - \mathbf{x}_b) \mathcal{F}_n^m(\mathbf{s}_B) + \delta \Psi_{A \rightarrow B}, \quad (3a)$$

$$\mathcal{F}_n^m(\mathbf{s}_B) = \sum_{k=0}^{p-n} \sum_{l=-k}^k \mathcal{M}_k^{l*}(\mathbf{z}_A) \Theta_{n+k}^{m+l}(\mathbf{s}_B - \mathbf{z}_A), \quad (3b)$$

$$\mathcal{M}_n^m(\mathbf{z}_A) = \sum_{a \in A} \mu_a \Upsilon_n^m(\mathbf{x}_a - \mathbf{z}_A). \quad (3c)$$

Here, p is the expansion order and $\delta \Psi_{A \rightarrow B}$ the error of the approximated potential. This expansion converges with increasing p if $\max_{a \in A} \{|\mathbf{x}_b - \mathbf{x}_a - \mathbf{r}|\} < |\mathbf{r}|$ with $\mathbf{r} \equiv \mathbf{s}_B - \mathbf{z}_A$.

Other important relations are those for the *multipoles* \mathcal{M}_n^m with respect to another expansion centre

$$\mathcal{M}_n^m(\mathbf{z}') = \sum_{k=0}^n \sum_{l=-k}^k \Upsilon_k^{l*}(\mathbf{z} - \mathbf{z}') \mathcal{M}_{n-k}^{m-l}(\mathbf{z}), \quad (3d)$$

and for the *field tensors* \mathcal{F}_n^m of the local expansion (3a) with respect to another expansion centre

$$\mathcal{F}_n^m(\mathbf{s}') = \sum_{k=0}^{p-n} \sum_{l=-k}^k \Upsilon_k^{l*}(\mathbf{s} - \mathbf{s}') \mathcal{F}_{n+k}^{m+l}(\mathbf{s}). \quad (3e)$$

Moreover, the computation of the acceleration \mathbf{a} from the local expansion (3a) requires

$$\Psi_n^m(\mathbf{x}_b) = \sum_{k=0}^{p-n} \sum_{l=-k}^k \Upsilon_k^{l*}(\mathbf{s}_B - \mathbf{x}_b) \mathcal{F}_{n+k}^{m+l}(\mathbf{s}_B) + \delta \Psi_n^m, \quad (3f)$$

when $\mathbf{a} = \nabla \Psi_0^0 = -(\Re\{\Psi_1^1\}, \Im\{\Psi_1^1\}, \Psi_1^0)$. Finally, the gravity generated from a source distribution with given multipoles is given by

$$\Psi_n^m(\mathbf{x}_b) = \sum_{k=0}^{p-n} \sum_{l=-k}^k \mathcal{M}_k^{l*}(\mathbf{z}_A) \Theta_{n+k}^{m+l}(\mathbf{x}_b - \mathbf{z}_A) + \delta \Psi_n^m. \quad (3g)$$

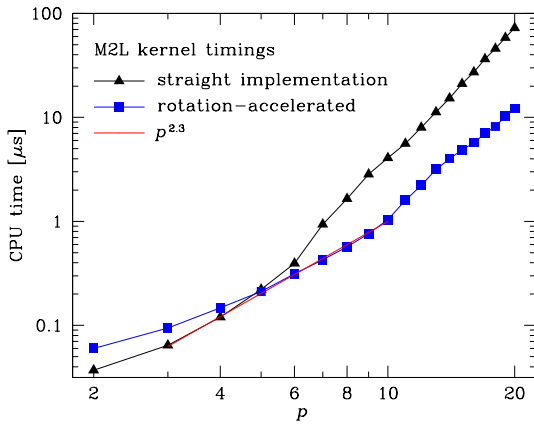


Fig. 1 Timings for the M2L kernel (using double precision without vectorisation) as function of expansion order p . The rotation accelerated version of Appendix A.6.2 is faster than the direct implementation of equation (3b) for $p \geq 5$.

Table 1 The FMM kernels. The tree code replaces direct summation (P2P) with P2M-M2M-M2P, while FMM uses P2M-M2M-M2L-L2L-L2P, see also Fig. 2. The P2L kernel corresponds to equation (3b) with $\mathbf{z}_A \rightarrow \mathbf{x}_a$ and $\mathcal{M}_k^1 \rightarrow m_a \delta_{k0}$, i.e. $\mathcal{F}_n^m(\mathbf{s}_B) = m_a \Theta_n^m(\mathbf{s}_B - \mathbf{x}_a)$.

name	meaning	equation
P2P	particle to particle	(1)
P2M	particle to multipole	(3c)
M2M	multipole to multipole	(3d)
M2P	multipole to particle	(3g)
M2L	multipole to local expansion	(3b)
P2L	particle to local expansion	see table caption
L2L	local expansion to local expansion	(3e)
L2P	local expansion to particle	(3f)

Relations (3b), (3d), and (3e) are equivalent to the much more complicated equations (17), (13), and (21) of Cheng, Greengard, and Rokhlin (1999, given without derivation)¹.

There are $(p+1)^2$ independent real-valued numbers \mathcal{F}_n^m (as well as \mathcal{M}_n^m , see also Appendix A.5.2), and their computation via equations (3b), (3d), and (3e) requires $\mathcal{O}(p^4)$ operations². These operation counts can be reduced to $\mathcal{O}(p^3)$ by rotating \mathbf{r} into the z direction (see Appendix A.6). Fig. 1 plots the time required per interaction computation as function of expansion order p , showing an effective $p^{2.3}$ scaling of the computational costs at $p \leq 10$, shallower than the $\mathcal{O}(p^3)$ asymptote.

¹ Cheng et al's expressions are quite cumbersome because they are given in terms of the surface spherical harmonics Y_n^m in polar coordinates and because they contain phase-factors like $i^{|m|-m}$ owing to their unconventional definition for the Y_n^m which implies $Y_n^{-m} = Y_n^{m*}$ instead of $Y_n^{-m} = (-1)^m Y_n^{m*}$.

² Expressions like $\mathcal{O}(p^n)$ for the operation count relate to the asymptotic behaviour at large expansion orders p . While this is straightforward to specify, it is not necessarily very relevant, since in the range up to $p \sim 10$, as required in practice, the actual costs usually grow more slowly than implied by the asymptotic behaviour (see Fig. 1 for a typical example) and because the numerical implementation may be data-dominated rather than computation dominated.

2.2 Algorithmic approach

2.2.1 The tree code: walking the tree

Let us first consider the tree code, which also uses the multipole expansion but is algorithmically simpler than FMM. The basic data structure is a hierarchical tree of spatial cells, which are either cubic with eight daughters cells (oct-tree) or cuboidal with two daughters (binary tree). In a first step, the multipoles \mathcal{M}_n^m have to be computed for each cell from those of their daughter cells, using the M2M kernel (equation 3d, see also Table 1), or (in case of final cells) of their particles, using the P2M kernel (equation 3c).

Next, the force for each sink position is computed using a separate *tree walk* starting with the root cell. The force generated by a cell C is computed via its multipole expansion, using the M2P kernel (equation 3g), if a *multipole-acceptance criterion* is met, i.e. if the cell is considered to be *well-separated* from the sink position. Otherwise, the cell is opened: the force is computed as the sum of the forces generated by the daughters cells (recursing if necessary). Thus, the tree code replaces direct summation's P2P kernel with the P2M, M2M, and M2P kernels, see the left panel of Fig. 2 for a schematic view.

2.2.2 FMM: the dual tree walk

An adaptive FMM algorithm also uses a hierarchical tree data structure. As with the tree code, the cell multipoles \mathcal{M}_n^m have to be precomputed for every cell in a first step.

Next, the forces for *all* sink positions and generated by *all* source particles are approximated using a single *dual tree walk* (Dehnen, 2002). This algorithm considers cell \rightarrow cell interactions and starts with the root \rightarrow root interaction. If the interacting cells are well separated, the interaction is approximated using the M2L kernel (equation 3b), which computes and accumulates the local field tensors $\mathcal{F}_n^m(\mathbf{s}_B)$ for the expansion of gravity within the sink cell B and due to all sources within the source cell A (in a mutual version of the algorithm, the interactions $A \rightarrow B$ and $B \rightarrow A$ are considered simultaneously). Otherwise, the interaction is split, typically into those between the daughters of the larger of the two interacting cells with the smaller.

Finally, the local field tensors $\mathcal{F}_n^m(\mathbf{s})$ are passed down the tree using the L2L kernel, and the local expansions are evaluated at the sink positions using the L2P kernel. Thus, the FMM replaces the M2P kernel of the tree code with the M2L, L2L and L2P kernels, see also Fig. 2.

Of course, in both tree code and FMM, direct summation (P2P kernel) is used whenever computationally preferable, i.e. for interactions involving only a few sources and sinks.

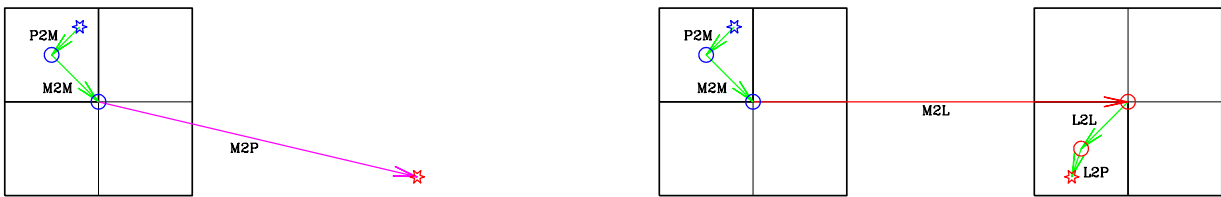


Fig. 2 **Left:** the tree code approximates the force from a source particle (blue star) at a sink position (red star) using the P2M and M2M kernels (green arrows) to compute the multipoles at the cell centres (blue circles) followed by the M2P kernel (pink arrow). The P2M and M2M kernels are called once per source particle and cell, respectively, while the M2P kernel is called many times for each sink position. **Right:** FMM replaces the M2P kernel by the M2L kernel (red arrow) followed by the L2L and L2P kernels (green arrows). Again, the L2L and L2P kernels are called once per sink cell and particle, respectively, but a single M2L kernel replaces many M2P kernels of the tree code, because it accounts for *all* sink positions within the sink cell.

3 Quantifying the approximation accuracy

Before the method can be optimised for accuracy, a sensible quantitative measure for this accuracy is needed as well as an acceptable value for this measure.

With direct-summation, the accuracy is limited only by the finite precision of computer arithmetic (round-off error). If double (64-bit) precision is not used throughout, it is customary to use the conservation of the total energy for quality control (e.g. Gaburov et al, 2009). However, as shown in Appendix B, the relative energy error is much smaller than the typical relative force error, simply because it is an average over many force errors. Even worse, the computation of the total energy, required for measuring its error, typically incurs a larger error. Thus, any measured non-conservation of the total energy is dominated by measurement error rather than true non-conservation due to acceleration errors.

With the tree code and FMM, the situation is subtly different, as discussed in Appendix B.3. Here, the measured non-conservation of energy actually reflects the amplitude of the acceleration errors in an average sense. However, an average measure for the effect of approximation errors cannot reflect their effect on the correctness of the simulation. For example, a single large force error has hardly any effect on the energy conservation but may seriously affect the validity of the simulation. While this latter goal is difficult to quantify, it is certainly better to consider the whole distribution of acceleration errors and pay particular attention to large-error outliers, than merely monitor an average.

3.1 Scaling acceleration errors

Obviously, the absolute errors $\delta a = |\mathbf{a}_{\text{computed}} - \mathbf{a}_{\text{true}}|$ are not very useful by themselves and must be normalised to be meaningful. One option is to divide δa by some mean field strength \bar{a} . While this makes sense for the average particle, it fails for those in the outskirts of the stellar system, where the field strength diminishes well below its mean.

To overcome such issues, a natural choice is the relative error $\delta a/a$. However, this is still problematic in the cen-

tre of a stellar system, where forces from the outward lying parts largely cancel. In such a situation, a can be small and hence the relative error large, even if each individual pairwise force has been computed with high accuracy. One option for avoiding this problem is – in analogy to the error estimate of numerical quadrature in case of an integrand oscillating around zero – to normalise δa with the sum

$$f_b \equiv \sum_{a \neq b} \frac{G\mu_a}{|\mathbf{x}_a - \mathbf{x}_b|^2} \quad (4)$$

of the absolute values of all pair-wise accelerations. In general $f_b \geq a_b$, while in the outskirts of a stellar system $f \rightarrow a \approx GM/r^2$ such that the *scaled error* $\delta a/f$ approaches the relative error $\delta a/a$ as desired. Conversely, in the centre $f \gg a$ (for a Plummer sphere, for example, $f \rightarrow 2GM/r_s^2$ as $r \rightarrow 0$ in the continuum limit) and $\delta a/f$ behaves sensibly if $a \rightarrow 0$.

3.2 The acceleration errors of direct summation

In order to assess the errors currently tolerated in collisional N -body simulations, the GPU-based direct-summation library *sapporo* (Gaburov et al, 2009) was applied to two sets of, respectively, $N = 10^5$ and $N = 10^6$ equal-mass particles, drawn randomly from a Plummer (1911) sphere (without any outer truncation). Fig. 3 shows the resulting distributions of acceleration errors as compared to direct summation in double (64bit) precision. As expected, the typical relative (or scaled) error is $\sim 10^{-7}$, comparable to the relative round-off error of single-precision floating-point arithmetic. However, there is a clear tail of large relative errors (middle panel). This is due to particles at small radii, whose acceleration is small, because the pair-wise forces with other particles mostly cancel out, while the (round-off) errors accumulate.

There is a significant increase in the error amplitude with particle number N : the errors for $N = 10^6$ are on average $\sim \sqrt{10}$ larger than for $N = 10^5$. This worrying property suggests that the fidelity of simulations using *sapporo* diminishes with N , implying that using this library with $N \gtrsim 10^7$ is not advisable.

From this exercise I conclude that in practice relative (or scaled) acceleration errors with an rms value of a few

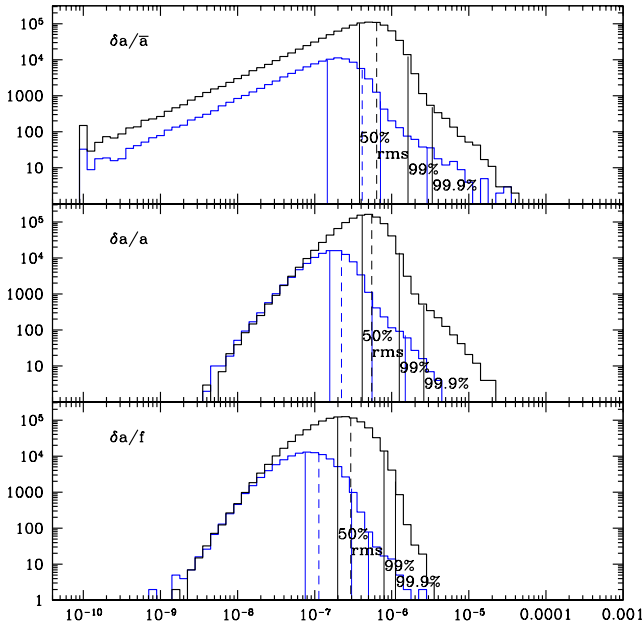


Fig. 3 Distribution of acceleration errors δa_i for $N = 10^5$ (blue) and $N = 10^6$ (black) particles drawn from a Plummer sphere when using the state-of-the-art GPU-based direct-summation library *sapporo* (version 1.6) as compared to direct summation in double (64bit) precision. The top, middle, and bottom panel refer to, respectively, the normalised (by the mean acceleration \bar{a}), relative, and scaled (by f defined in equation 4) acceleration errors. The thin vertical lines indicate the rms error (dashed) as well as the median and the 99 and 99.9 percentiles (solid). Bins are 0.1 dex wide.

10^{-7} and maximum ~ 10 times larger are accepted in N -body simulations of collisional stellar dynamics.

4 Assessing the approximation errors

In order to optimise any implementation of FMM for high accuracy and low computational costs, a good understanding of and accurate estimates for the errors incurred by each individual FMM interaction are required. To this end, I now perform some numerical experiments.

I create a Plummer sphere of $N = 10^6$ particles and build an oct-tree. For each cell, the centre \mathbf{z}_{ses} of the smallest enclosing sphere for all its particles is found (see Section 5.1.1). I use $\mathbf{z} = \mathbf{s} = \mathbf{z}_{\text{ses}}$ for each cell and pre-compute the cells' multipole moments $\mathcal{M}_n^m(\mathbf{z})$. Finally, the dual tree walk is performed using the multipole-acceptance criterion

$$\theta < \theta_{\text{crit}} \quad (5)$$

with the *opening angle*

$$\theta \equiv (\rho_{\mathbf{z},A} + \rho_{\mathbf{s},B})/r, \quad r \equiv |\mathbf{s}_B - \mathbf{z}_A|. \quad (6)$$

Here, for each cell C

$$\rho_{\mathbf{z},C} \equiv \max_{\text{sources } a \in C} \{|\mathbf{x}_a - \mathbf{z}_C|\} \quad \text{and} \quad (7)$$

$$\rho_{\mathbf{s},C} \equiv \max_{\text{sinks } b \in C} \{|\mathbf{x}_b - \mathbf{s}_C|\} \quad (8)$$

are (approximations for) the radii of the smallest spheres centred on \mathbf{z} and \mathbf{s} and containing all sources and sinks, respectively. In the experiments of this section $\rho_{\mathbf{z}} = \rho_{\mathbf{s}}$ for each cell, because $\mathbf{z} = \mathbf{s}$ and because all particles are source and sink simultaneously, but in general $\rho_{\mathbf{z}}$ and $\rho_{\mathbf{s}}$ may differ.

With the simple criterion (5) the multipole expansion is guaranteed to converge and have bounded errors³. Cell \rightarrow cell interactions with $N_A N_B < p^3$, cell \rightarrow particle interactions with $N_C < 4p^2$, and particle \rightarrow cell interactions with $N_C < p^2$ are ignored, because direct summation is faster than FMM and will be preferred in a practical application. For the remaining well-separated interactions, the accelerations of all particles within the sink cell and due to all particles within the source cell are computed using both FMM and direct summation (with 64-bit precision for both). I then evaluate for each sink particle the acceleration error

$$\delta a \equiv |\mathbf{a}_{\text{fmm}} - \mathbf{a}_{\text{true}}| \quad (9)$$

with \mathbf{a}_{true} obtained by direct summation in double precision.

4.1 Cell-cell interactions

Cell-cell interactions involve the M2L kernel of the P2M + [M2M] + M2L + [L2L] + L2P chain of kernels. They are by far the most common and most important of all interactions encountered in the dual tree walk. For a random subset of cell-cell interactions generated by my experiments, the top panel of Fig. 4 plots the maximum (over all particles within the sink cell) of δa normalised by the average acceleration M_A/r^2 against θ , while the bottom panel plots the maximum relative force error $\delta a/a$. As expected, the errors decrease with smaller θ and increasing p , though there is substantial scatter at any given θ and p . At $\theta \sim 1$, the expansion order has little effect on the errors, implying that $\theta \ll 1$ is required for small errors.

4.1.1 Comparing with simple error estimates

The approximation error from a single FMM interaction with $\theta < 1$ has the theoretical strict upper bound (Dehnen, 2002)

$$\delta a \leq \frac{M_A}{r^2} \frac{(p+1)\theta^p}{(1-\theta)^2}, \quad (10)$$

which is plotted as thin curves in the top panel of Fig. 4. Obviously, this upper bound is satisfied, but typically it is 10-100 times larger than the actual largest error.

Moreover, equation (10) predicts diverging errors for $\theta \rightarrow 1$, while the actual errors behave much nicer. This is presumably because diverging errors only occur for rare sink positions combined with extreme source distributions (such

³ The original definition used in the tree code of Barnes and Hut (1986) did not ensure bounded errors, causing the infamous ‘exploding galaxies’ bug first reported by Salmon and Warren (1994).

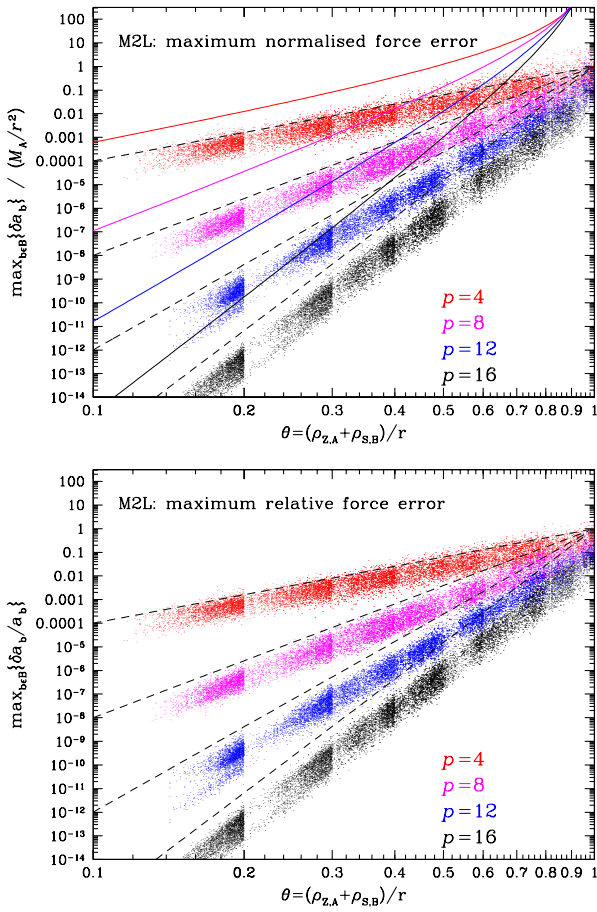


Fig. 4 Results of the experiments of Section 4.1. Each point represents a single cell \rightarrow cell interaction with expansion order p as indicated. The maximum of the relative (bottom) and absolute force error (top; normalised to the mean force M_A/r^2) within the sink cell is plotted against the opening angle θ . The curves in the top panel correspond to the relation (10), while the dashed lines are the power laws θ^p .

as all particles concentrated near one point at the edge of the source sphere), which are not realised in these experiments (but see Fig. 7).

Fig. 4 also shows as dashed lines the simple power laws θ^p , which give closer, though not strict, bounds

$$\delta a \lesssim \theta^p M_A/r^2 \quad \text{and} \quad \delta a/a \lesssim \theta^p \quad (11)$$

to the actual errors.

4.1.2 Better error estimates

The simple error estimates (11) are still quite inaccurate: the maximal error is often much smaller (see also the dashed histograms in Fig. 5). The offsets in Fig. 4 of θ^p from the actual errors increase with p . This effect vanishes if the same limit for $N_A N_B$ is used for all p , suggesting that it is caused by smoother distributions for larger numbers N_A of sources. Indeed, if I simply divide the estimates (11) by $\sqrt{N_A}$ the

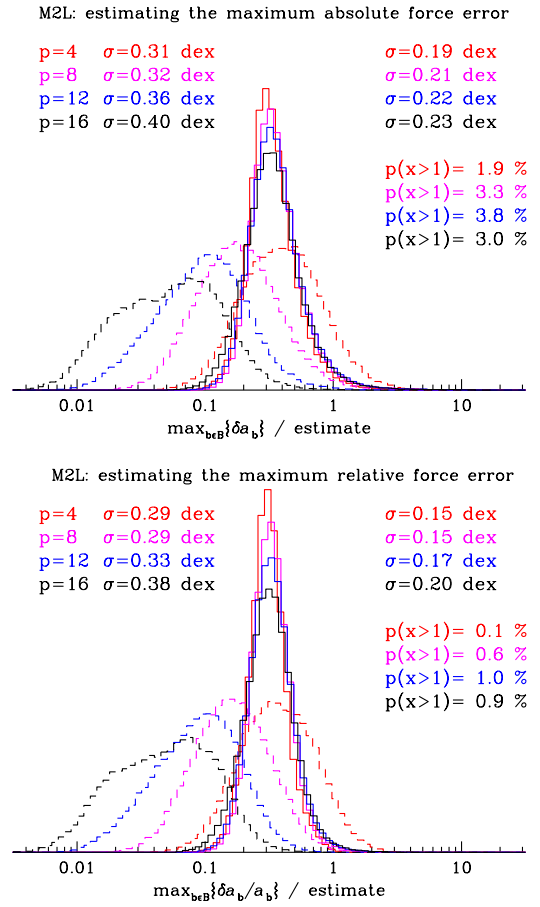


Fig. 5 Distributions of the ratio of the maximum absolute (top) and relative (bottom) force error to either the simple estimates (11) (dashed, σ on the left) or the improved estimates (14) (solid, σ on the right) for the cell-cell interactions of Fig. 4. The reported probabilities for error underestimation refer to the improved estimates. Vertical scale is linear in the number of interactions.

scatter of the residuals is much reduced, but a systematic trend with p remains.

However, there is more information about the distribution of sources than merely their number: their multipole moments \mathcal{M}_n^m for $n \leq p$. In order to incorporate this information into an error estimate, I first compute for each cell the multipole power

$$\mathcal{P}_n^2 \equiv \sum_{m=-n}^n (n-m)!(n+m)! |\mathcal{M}_n^m(\mathbf{z})|^2. \quad (12)$$

By design these (i) satisfy $\mathcal{P}_{n,A} \leq M_A \rho_{z,A}^n$ for any distribution of sources; (ii) are invariant under rotation (of the coordinate system) and hence independent of the interaction direction; and (iii) provide an upper bound for the amplitude of the multipole: $|\mathcal{M}_n^m(\mathbf{z})| \leq \mathcal{P}_n/n!$. Having computed \mathcal{P}_n for each source cell, one can evaluate

$$E_{A \rightarrow B} \equiv \frac{1}{M_A} \sum_{k=0}^p \binom{p}{k} \frac{\mathcal{P}_{k,A} \rho_{z,B}^{p-k}}{r^p}. \quad (13)$$

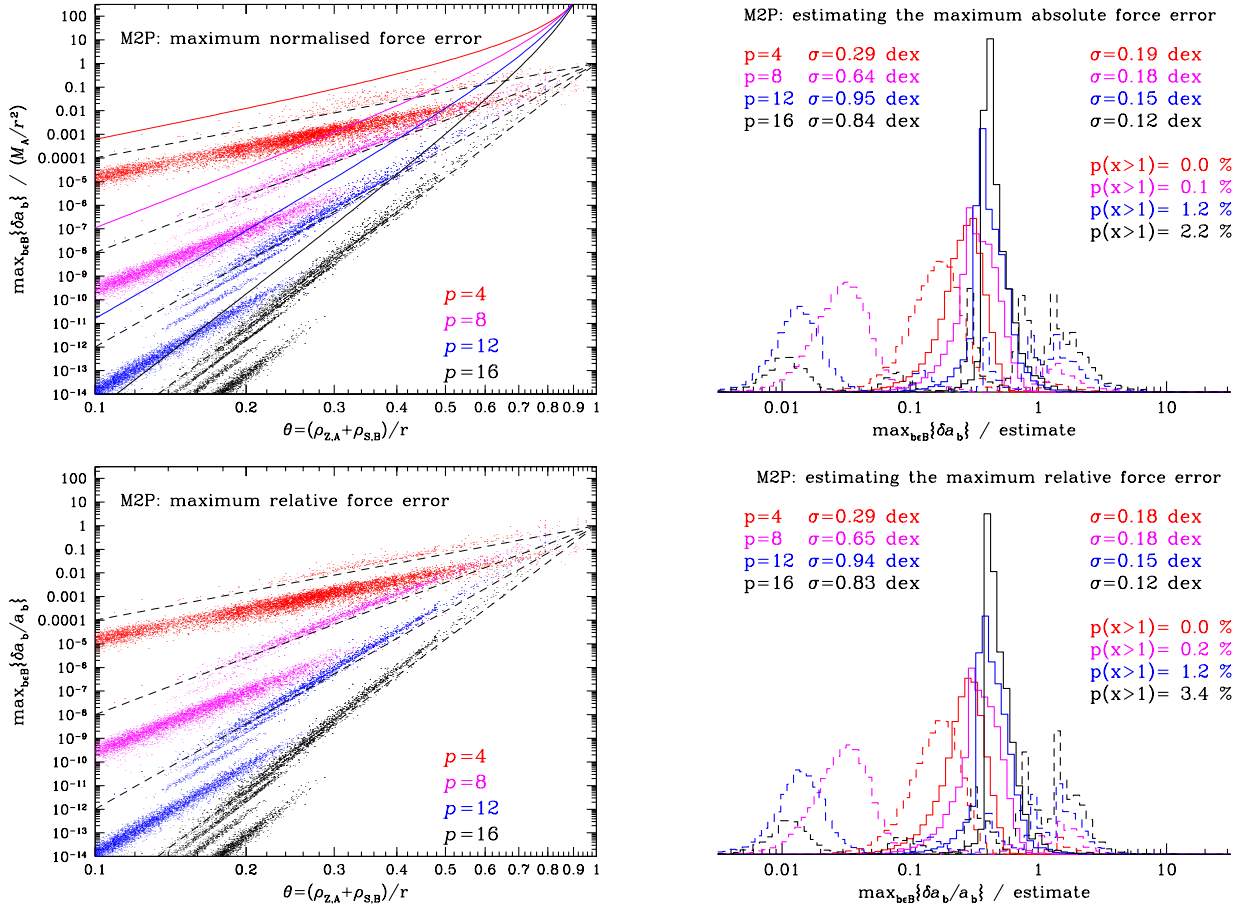


Fig. 6 As Fig. 4 (left) and Fig. 5 (right) but for cell \rightarrow particle interactions, see Section 4.2.1.

with $\mathcal{O}(p)$ operations. Note that $E_{A \rightarrow B} \leq \theta^p$ with equality only for $\mathcal{P}_{n,A} = M_A \rho_A^n$. The new error estimates are then

$$\delta a \lesssim \tilde{E}_{A \rightarrow B} \frac{M_A}{r^2} \quad \text{and} \quad \frac{\delta a}{a} \lesssim \tilde{E}_{A \rightarrow B} \quad (14)$$

with

$$\tilde{E}_{A \rightarrow B} = \frac{8 \max\{\rho_{z,A}, \rho_{s,B}\}}{\rho_{z,A} + \rho_{s,B}} E_{A \rightarrow B}. \quad (15)$$

In Fig. 5, these new error estimates are compared with the simple estimates (11) of the last subsection by displaying the distributions of the ratio of the actual maximum error to these estimates. The main difference between the two sets of estimators is their accuracy: there is much less scatter for the new (solid histograms) than for the old estimators (dashed). Consequently, there are hardly any interactions for which the force error is overestimated by more than a factor ten, while the simple estimators (11) overestimated the force error by more than that for many interactions, in particular at large p . Another remarkable property of the new error estimator is its consistency with respect to expansion order: there is no systematic drift with expansion order.

The number of underestimated force errors (abscissa > 1 in Fig. 5) is small but there is a clear tail of underestimated

absolute errors (top panel). As this is not present for the relative errors, it must be caused by the deviation of the acceleration from the mean M_A/r^2 . Indeed, the maximum error is expected to occur on the side of the sink towards the source, where the acceleration is larger, about $M_A/(r - \rho_{s,B})^2$. When accounting for this by simply replacing r in (14) with $r - \rho_{s,B}$, the tail of underestimated force errors is diminished, but the overall distributions widens and a tail of overestimated errors appears.

4.2 Particle-cell interactions

Just occasionally, the dual tree walk algorithm encounters particle-cell interactions. Most of them will be computed using direct summation, leaving only the few with populous cells for the FMM approximation.

For particle \rightarrow cell and cell \rightarrow particle interactions the FMM approximation uses the P2L and M2P kernels, respectively. Because these kernels correspond to the M2L kernel in the limits of $\rho_{z,A} \rightarrow 0$ and $\rho_{s,B} \rightarrow 0$, respectively, all the algebra developed in the previous sub-section still applies.

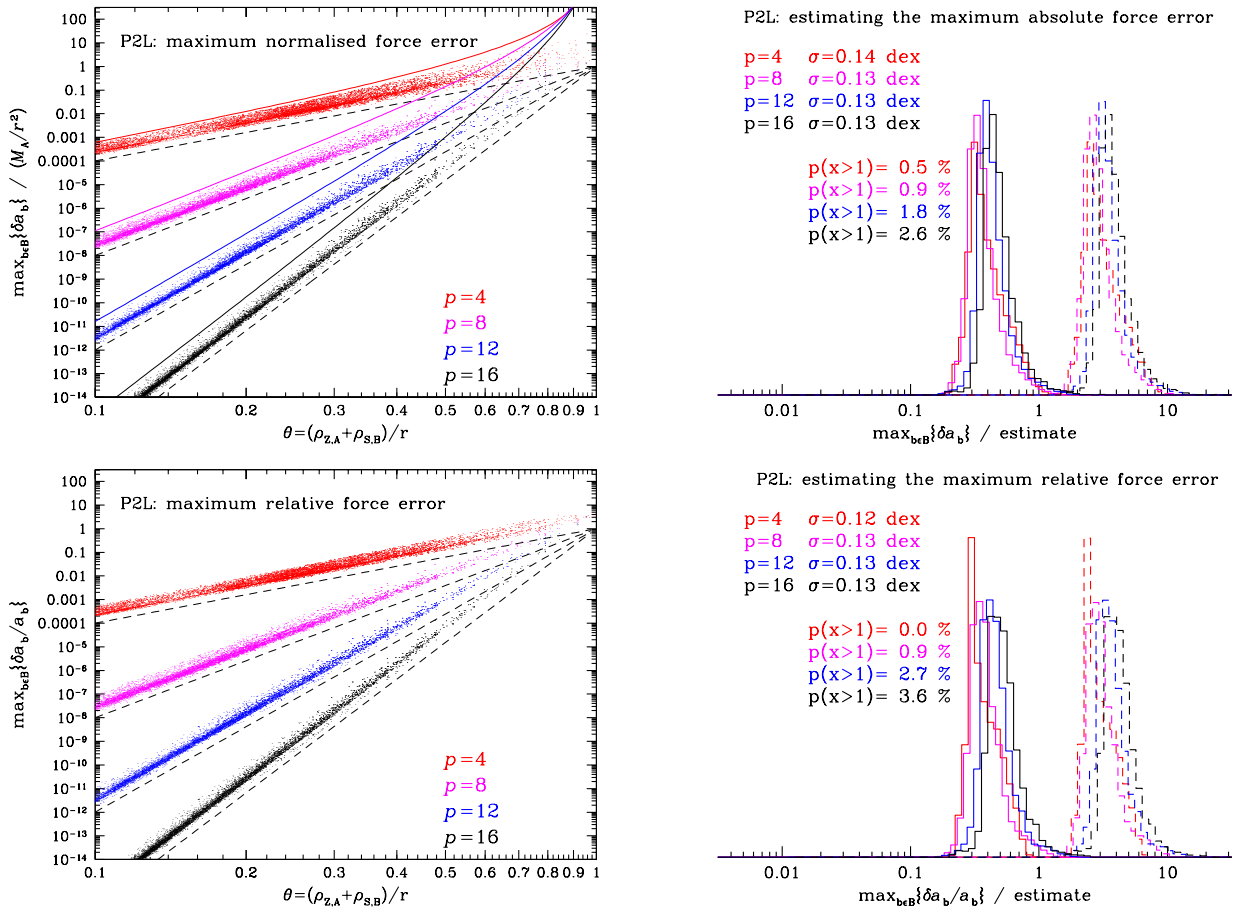


Fig. 7 As Fig. 4 (left) and Fig. 5 (right) but for particle \rightarrow cell interactions, see Section 4.2.2.

4.2.1 Cell \rightarrow particle interactions

The left panels of Fig. 6 are equivalent to Fig. 4 for cell \rightarrow particle interactions (which dominate in the tree code). The most notable difference to Fig. 4 is the streaky nature of the relations, implying a multi-modal distribution of errors at any given θ and p , as also evident from the dashed histograms in the right panels. The cause for this is simply that in an oct-tree cell size is quantised. In fact, the improved error estimates (14) account for this effect resulting in narrow mono-modal distributions of error offsets.

4.2.2 Particle \rightarrow cell interactions

The left panels of Fig. 7 are equivalent to Fig. 4 for particle \rightarrow cell interactions. Clearly, at any given θ and p , the errors are larger than for any other type of interactions and are in fact approaching the theoretical limit (solid curves in the top left panel). What is more, not much can be done about this in terms of error estimates: since the source is just a particle without inner structure, the improved estimates (14) are simply a rescaling by a factor 8 from the simple power laws (a simple shift between the dashed and solid histograms in the

right panels). They are nonetheless equally accurate as for the cell \rightarrow cell interactions and suffer from a similar level of force underestimation (for a few percent of interactions and by less than a factor two).

5 Optimising the multipole-acceptance criterion

With the improved error estimates in hand, the practical implementation of FMM for high accuracy can finally be considered. The main questions arising in this context are:

- what to pick for the expansion centres \mathbf{z} and \mathbf{s} ?
- when to consider two cells well-separated?
- what expansion order p to use?

The possible answers to these questions affect both the computational cost and the approximation accuracy. Hence, for a given accuracy target, there exists an optimal choice for all these parameters, in the sense of minimal CPU time (and memory) consumption. This section deals with the algorithmic aspects of this problem, i.e. the choice for \mathbf{z} and \mathbf{s} and the functional form of the multipole-acceptance criterion. The

tuning of the parameters (of the multipole-acceptance criterion as well as the expansion order) with the aim of minimal computational effort for a given accuracy is the subject of the next section.

Astonishingly, this issue of optimal choice for \mathbf{z} and \mathbf{s} and the multipole-acceptance criterion has not been much investigated. Instead, implementations of multipole methods often employ either of two simple strategies. The tree-code generally uses a fixed order p and an expansion centred on the cells' centres of mass, while two cells are considered well-separated if the simple geometric multipole-acceptance criterion (5) is satisfied, such that θ_{crit} controls the accuracy.

With traditional FMM, on the other hand, the expansion centres \mathbf{z} and \mathbf{s} are both taken to be the geometric cell centres and two cells are deemed well-separated as soon as the expansion converges, corresponding to $\theta_{\text{crit}} = 1$. When using hierarchical cubic grids (instead of an adaptive tree), this is implemented by interacting only between non-neighbouring cells on the same grid level whose parent cells are neighbours (e.g. Cheng et al, 1999). The accuracy is then only controlled by the expansion order p .

5.1 Choice of expansion centres \mathbf{z} and \mathbf{s}

As far as I am aware, all existing FMM implementations use the same position for the multipole and potential expansion centres, i.e. $\mathbf{z} = \mathbf{s}$, for each cell. For traditional FMM, these are equal to the geometric cell centres. This has the benefit of a finite number of possible interaction directions $\hat{\mathbf{r}}$, in particular when $\theta_{\text{crit}} = 1$, for which the coefficients $\Theta_n^m(\hat{\mathbf{r}})$ could be pre-computed. However, the computation of these coefficients on the fly is often faster than a table look-up. Moreover, in view of Fig. 4 $\theta_{\text{crit}} = 1$ appears ill-suited for high accuracy.

In fact, the restriction $\mathbf{z} = \mathbf{s}$ reduces the freedom and hence the potential for optimising the method. Nonetheless, when aiming for low accuracy, choosing $\mathbf{z} = \mathbf{s} = \mathbf{z}_{\text{com}}$, the cells' centres of mass, has some advantages. First, the dipoles vanish and the low-order multipoles tend to be near-minimal. Second, if using a mutual version of the algorithm (when the interactions $A \rightarrow B$ and $B \rightarrow A$ are done simultaneously), the computational costs are reduced and the approximated forces satisfy Newton's third law exactly, i.e. $\mathbf{F}_{ab} + \mathbf{F}_{ba} = 0$ (Dehnen, 2002).

However, in practice there is no benefit from such an exact obedience of Newton's law, as the total momentum is not exactly conserved, because of integration errors arising from the fact that the particles have individual time steps. Moreover, the degree of deviation from exact momentum conservation in such a case does not reflect the true accumulated force errors. In a more general method, the approximated forces will deviate from the ideal $\mathbf{F}_{ab} + \mathbf{F}_{ba} = 0$ by

an amount comparable to their actual force errors and the non-conservation of total momentum is somewhat indicative of the accumulated effect of the force errors (see also Appendix B.3).

5.1.1 Choice of the potential expansion centre \mathbf{s}

The results of Section 4, in particular the functional form of $E_{A \rightarrow B}$ in equation (13), suggest to choose the potential expansion centres \mathbf{s} such that the resulting sink radii $\rho_{\mathbf{s}}$, and hence the estimated interaction errors, are minimal. Thus, $\mathbf{s} = \mathbf{z}_{\text{ses}}$, the centre of the *smallest enclosing sphere*. Finding the smallest enclosing sphere for a set of n points has complexity $\mathcal{O}(n)$. Doing this for every sink cell would incur a total cost of $\mathcal{O}(N \ln N)$ and be prohibitively expensive.

Instead, I use an accurate approximation by finding for each cell the smallest sphere enclosing the spheres of its grand-daughter cells. This incurs a total cost of $\mathcal{O}(N)$ and is implemented via the Computational Geometry Algorithms Library (www.cgal.org, Fischer et al, 2013), using an algorithm of Matoušek, Sharir, and Welzl (1996).

5.1.2 Choice of the multipole expansion centre \mathbf{z}

As already mentioned above, setting $\mathbf{z} = \mathbf{z}_{\text{com}}$ has some virtue for low expansion orders p . However, for high expansion orders, the high-order multipoles become ever more important, suggesting that $\mathbf{z} = \mathbf{z}_{\text{ses}}$ may be a better choice. In order to assess the relative merits of these methods, I repeated the experiments of Section 4 for both methods and compared the resulting maximum absolute and relative force errors incurred for the *same* cell \rightarrow cell interactions (for which the two methods give different θ).

I found that the errors for the two methods are very similar with an rms deviation of ~ 0.15 dex, but a very small mean deviation. At $p \lesssim 8$ there is a trend of more accurate forces for $\mathbf{z} = \mathbf{z}_{\text{com}}$, while at $p \gtrsim 8$ $\mathbf{z} = \mathbf{z}_{\text{ses}}$ obtains smaller errors. This trend is simply a consequence of \mathcal{P}_k being smaller for $\mathbf{z} = \mathbf{z}_{\text{com}}$ than for $\mathbf{z} = \mathbf{z}_{\text{ses}}$ at low k and larger at high k . This together with the improved error estimates (14) also explains that (for an interaction $A \rightarrow B$) $\mathbf{z} = \mathbf{z}_{\text{com}}$ tends to give more accurate forces if $\rho_{\mathbf{z},A} < \rho_{\mathbf{s},B}$, while $\mathbf{z} = \mathbf{z}_{\text{ses}}$ tends to be more accurate if $\rho_{\mathbf{z},A} > \rho_{\mathbf{s},B}$.

5.2 A simple FMM implementation

Let us first experiment with an implementation that uses the simple multipole-acceptance criterion (5) and a fixed expansion order p . This is the standard choice for the tree code and as such implemented in many gravity solvers used in astrophysics. The computational costs of such an implementation roughly scale as $p^\alpha / \theta_{\text{crit}}^3$ with $\alpha \sim 2.3$, because the number of interactions increases as $\theta_{\text{crit}}^{-3}$ for large N , while

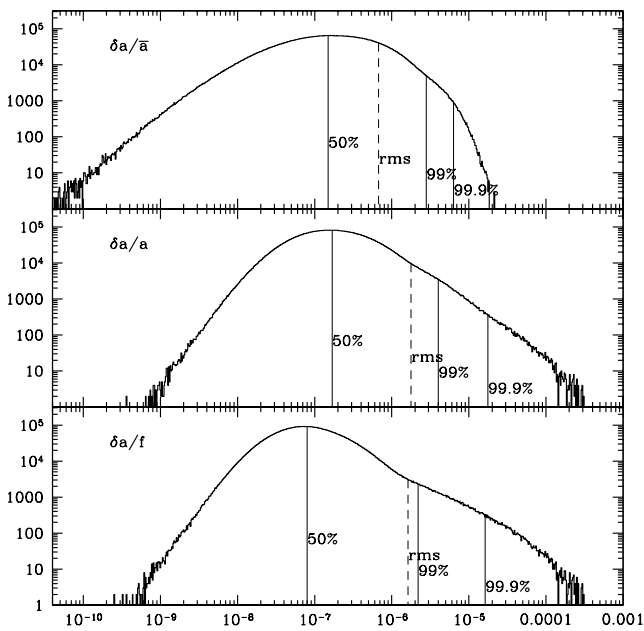


Fig. 8 Similar to Fig. 3, but for $N = 10^7$ particles and accelerations obtained by FMM using expansion order $p = 8$ and multipole-acceptance criterion $\rho_{z,A} + \rho_{s,B} < r\theta_{\text{crit}}$ (equation 5) with $\theta_{\text{crit}} = 0.4$. Bins are 0.01 dex wide.

the cost for one is $\propto p^{2.3}$. Together with the simple error estimate (11), this means that if one aims each FMM interaction to satisfy $\delta a/a < \epsilon$, then the minimum cost for fixed ϵ occurs for

$$\theta_{\text{crit}} = e^{-\alpha/3} \approx 0.46$$

Thus, the optimal opening angle is independent of p . The accuracy is then controlled by the expansion order, requiring $p \gtrsim 16$ for $\epsilon < 10^{-8}$ (according to Fig. 4). The computational costs rise roughly like $|\ln \epsilon|^\alpha$ with decreasing ϵ .

I applied the FMM method with $\mathbf{z} = \mathbf{z}_{\text{ses}}$, expansion order $p = 8$, and $\theta_{\text{crit}} = 0.4$ to $N = 10^7$ equal-mass particles drawn from a Plummer sphere. Fig. 8 plots the resulting distributions of absolute (top), relative (middle), and scaled (bottom) acceleration errors. All three distributions are monomodal, but very wide, much wider than those obtain from GPU-based direct summation (Fig. 3). In particular, there are extended tails towards very large relative or scaled errors, containing only $\lesssim 1\%$ of the particles but reaching up to 1000 times the median error. These tails are due to particles at large radii and, for the relative errors only, also at small radii (see the discussion in Section 3.1).

There are two main effects responsible for these properties of the error distributions. First, errors from a single FMM interaction follow a distribution with variance of 1–2 dex. The maximum errors reported in Section 4 only occur for particles near the edges and corners of the sink cell, while most have smaller errors. Moreover, the force errors due to FMM interactions of the same sink cell with source cells in

opposing directions tend to partially cancel rather than add up. Both explain why the median errors reported in Fig. 8 are much smaller than the maximum relative error incurred by a single cell \rightarrow cell interaction, which according to Fig. 4 is $\sim 10^{-4}$.

More important is a second effect: the final force errors are not the sum of the relative errors of individual FMM interactions, which are controlled by the simple multipole-acceptance criterion, but of their *absolute* errors δa . Since, according to equation (11), $\delta a \sim \theta^p M_A / r^2 \sim \theta^{p+2} M_A / 4\rho_{z,A}^2$, the FMM interactions with cells of large surface density M/ρ_z^2 dominate the error budget. In fact, the particles at very large radii have $\delta a/a \approx \delta a/f \sim 10^{-4}$, exactly as expected from a few FMM interactions with near maximal errors.

5.3 Towards better multipole-acceptance criteria

This discussion suggests that multipole-acceptance criteria which balance the absolute force errors of individual FMM interactions are preferable. When working with the simple estimators (11) or the error bound (10), this leads to critical opening angles which depend on the properties of the interacting cells, such as their mass or surface density.

Such an approach can indeed be made to work (Dehnen, 2002), but the aim here is to go beyond that and use the improved error estimates (14). This results in the multipole-acceptance criteria

$$\theta < 1 \wedge \tilde{E}_{A \rightarrow B} \frac{M_A}{r^2} < \epsilon \min_{b \in B} \{a_b\}, \quad (16a)$$

$$\theta < 1 \wedge \tilde{E}_{A \rightarrow B} \frac{M_A}{r^2} < \epsilon \min_{b \in B} \{f_b\} \quad (16b)$$

with the aim to obtain $\delta a/a \lesssim \epsilon$ and $\delta a/f \lesssim \epsilon$, respectively.

The black histograms in Fig. 9 show the error distributions resulting from these criteria, when the values for a_b and f_b used in equations (16) have been taken from the direct-summation comparison run. The distributions for $\delta a/a$ in the left and $\delta a/f$ in both panels are remarkably narrow with a median error $\sim \epsilon$ as targeted, a steep truncation towards large errors, and a maximum error $\sim 10\epsilon$. The tail of large $\delta a/a$ in the right panel is due to particles at small radii, for which $a \ll f$ such that criterion (16b) allows large $\delta a/a$.

The difference between these error distributions and those shown in Fig. 8 and resulting from the simple geometric multipole-acceptance criterion (5) is remarkable. While the median errors are comparable, the criteria (16) do not produce extended tails of large errors of the quantity controlled ($\delta a/a$ in left and $\delta a/f$ in the right panels of Fig. 9), and the maximum errors are more than 2 orders of magnitude smaller. What is more, the tails towards small errors have also been somewhat reduced, indicating that the improved criterion avoids overly accurate individual FMM interactions.

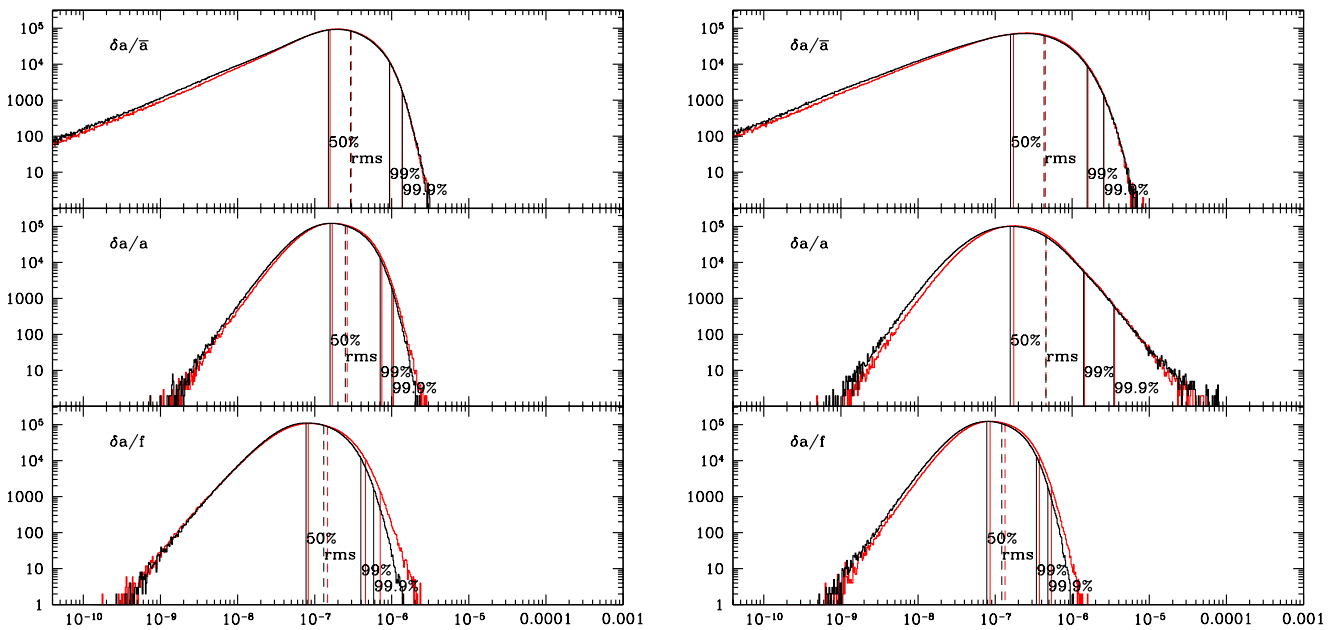


Fig. 9 Same as Fig. 8 but for the multipole-acceptance criterion (16a) with $\varepsilon = 2 \times 10^{-7}$ (left) or (16b) with $\varepsilon = 10^{-7}$ (right). The values for a and f are either taken from the direct-summation run (black), or obtained by low-order FMM (red, see section 5.4.2). In all cases the computational effort is similar to that of the FMM run shown in Fig. 8 (since $a \leq f$ criterion (16a) gives a tighter constraint than (16b) and hence requires larger ε for the same computational effort).

This improvement has been achieved without increasing the overall computational effort, but by carefully considering the error contribution from each approximated interaction.

5.4 Practical multipole-acceptance criteria

In a real application one has, of course, no a priori knowledge of a_b or f_b for any particle and must instead use something else in the multipole-acceptance criteria (16). In some situations, a suitable scale can be gleaned from the properties of the system modelled. For example, if simulating a star cluster of known mass profile $M(r)$ and centre \mathbf{x}_0 , one may simply use $a_b \sim GM(r_b)r_b^{-2}$ with $r_b = |\mathbf{x}_b - \mathbf{x}_0|$. I now consider other options.

5.4.1 Using accelerations from the previous time step

Employing the accelerations \mathbf{a}_b from the previous time step in equation (16a) requires no extra computations. However, it means that the gravity solver is not self-contained, but requires some starter to get the initial accelerations.

Also, using information from the previous time step subtly introduces an artificial arrow of time into the simulation, because $\delta a_{\text{new}} < \varepsilon a_{\text{old}}$ implies $\delta a_{\text{new}}/a_{\text{new}} < \varepsilon a_{\text{old}}/a_{\text{new}}$. Hence, a particle moving in a direction of increasing acceleration has, on average, smaller $\delta a/a$ than when moving in the opposite direction, or in reversed time. However, the

time integration methods currently employed almost exclusively in N -body simulations of collisional stellar dynamics are irreversible and introduce their own arrow of time. This suggests, that the additional breach of time symmetry by the magnitude (not the direction) of the force error may not be a serious problem in practice⁴.

5.4.2 Estimating a_b or f_b using low-order FMM

As Section 4 has shown, the error estimate $\tilde{E}_{A \rightarrow B}$ used in the multipole-acceptance criteria (16) still has significant uncertainty, and using highly accurate values for a_b or f_b in equations (16) is unnecessary. Instead, rough estimates should suffice. Such estimates can be obtained via a low-order FMM. This amounts to running the FMM twice: once with a simple multipole-acceptance criterion to obtain rough estimates for a_b or f_b , and then again using the sophisticated criteria (16) employing the results of the first run.

The acceleration scale f (defined in equation 4) is similar to the gravitational potential (1), except that its Greens function is $|\mathbf{r}|^{-2}$. This implies that it too can be estimated using FMM, albeit not using an explicitly harmonic formulation.

I implemented both options, estimating \mathbf{a} or f via FMM, using the lowest possible order ($p = 0$ for f and $p = 1$ for gravity—recall that $\mathbf{a} = \nabla \Psi$ is approximated at one order

⁴ The situation is different for N -body simulations of collisionless stellar dynamics, where reversible integrators are used and the accepted force errors, and thus their time asymmetries, are significantly larger.

lower than the potential Ψ) and multipole-acceptance criterion $\theta < 1$. To this end, I use $\mathbf{s} = \mathbf{z} = \mathbf{z}_{\text{com}}$ and a mutual version of the dual tree walk. The resulting estimates for f or $a = |\mathbf{a}|$ have rms relative errors of $\sim 15\%$. The additional computational effort is still much smaller than that of the high-accuracy approximation of gravity itself, though estimating f is faster because it is a scalar rather than a vector and because no square-root needs to be calculated.

The distributions of acceleration errors resulting from using these estimates in equations (16) are shown in red in Fig. 9. They are only very slightly worse than those in black, which have been obtained using the exact values of a_b and f_b in equations (16).

6 Optimising adaptive FMM

The previous section provided answers to the first two questions asked at its beginning, but not to the one after the optimal expansion order p . To answer this question I now report on some experiments, which also provide the actual computational costs for a given required force accuracy.

All experiments are run on a single compute node with 16 Intel Xeon E5-2670 CPUs, which support the AVX instruction set (see below), and using code generated by the gcc compiler (version 4.8.2).

6.1 Implementation details

The FMM relations of Section 2 and Appendix A (using the rotation-accelerated M2L kernel of Appendix A.6 when faster) have been implemented in computer code. The code employs a one-sided version of the dual tree walk, which considers the interactions $A \rightarrow B$ and $B \rightarrow A$ independently. The code is written in the C++ programming language and has been tested using various compilers and hardware. The implementation employs vectorisation and shared-memory parallelism as outlined below.

6.1.1 Vectorisation

Most current CPUs support vector sizes of 16 (SSE), 32 (AVX), or 64 (MIC) bytes, allowing $K = 2, 4,$ or 8 identical simultaneous double-precision floating-point operations (or twice as many in single precision). Because the FMM kernels do not (usually) relate adjacent elements, their efficient vectorisation is not straightforward (and well beyond compiler optimisation). I explicitly implement a method computing K M2L kernels simultaneously. To this end, the multipole moments of the K source cells are loaded into a properly aligned buffer (similar to transposing a matrix) before,

and afterwards the K field tensors are added from their vector-buffer to the sink cells' field tensors. Unfortunately, this loading and storing (which cannot be vectorised) reduces the speed-up obtained by the simultaneous kernel computations.

Conversely, direct summation is perfectly suitable for vectorisation and a speed-up of a factor K is achievable. The code prefers direct summation whenever this is deemed to be faster, based on a threshold for the number of particle-particle interactions 'caught' in a given cell-cell interaction.

6.1.2 Multi-threading

All parts of the implementation use multi-threading and benefit from multi-core architectures. This is done via hierarchical task-based parallelism implemented via *threading building blocks* (tbb, Reinders, 2007), an open source task parallel library with a work-stealing scheduler. The algorithms for multi-threaded tree building and dual tree walk are quite similar to those described by Taura et al (2012) and I refrain from giving details here.

6.1.3 Precision and expansion order

This study reports only on one particular implementation aimed at high accuracy. It uses double precision (64 bits) floating-point arithmetic throughout, $\mathbf{z} = \mathbf{z}_{\text{ses}}$, and expansion orders $p \leq 20$.

6.2 Wall-clock time versus accuracy

I applied my implementation with criteria (16a) and (16b) to $N = 10^7$ particles drawn from a Plummer sphere, and using low-order estimates for a_b and f_b in equations (16). I varied the expansion order p and the accuracy parameter ϵ and for each run plot in Fig. 10 the total wall-clock time against the rms and the 99.99 percentile acceleration errors.

The rms error is always ten times smaller than the 99.99 percentile⁵, implying the absence of extended large-error tails. For any fixed expansion order p , the relation between time and error can be approximated by a constant plus a power law that becomes flatter for larger p . At any given error, there is an optimal expansion order p in the sense of providing the fastest approximation. When using this optimal expansion order, the fastest FMM computation for a given error scales very nearly like a power law with exponent ~ -0.18 . Thus when reducing the error by a factor ten, the computational costs rise only by a factor ~ 1.5 .

Constraining the relative error (top panel of Fig. 10) is slightly more costly than constraining the scaled error (bottom panel). This is largely because $f > a$ as discussed in the

⁵ The increase of this ratio to ≈ 20 towards small errors may well be caused by inaccuracies of the direct summation used for calculating the errors.

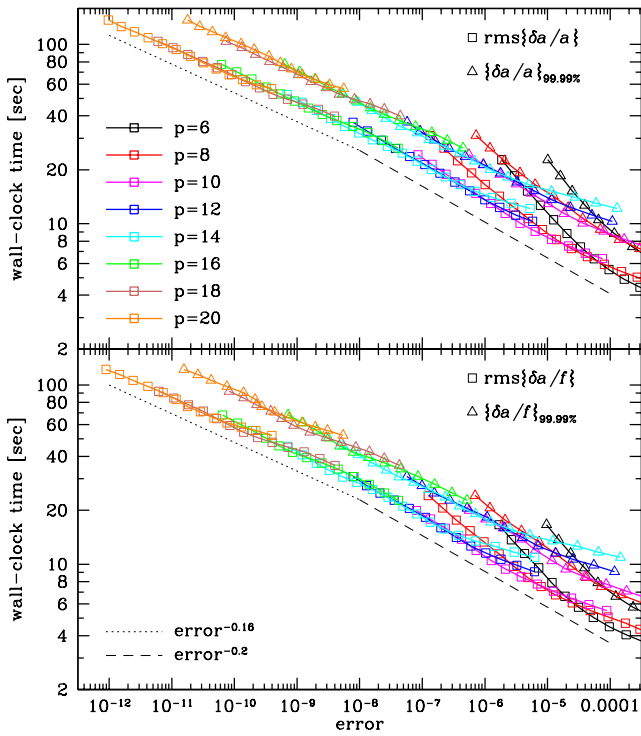


Fig. 10 Wall-clock time versus relative (top) and scaled (bottom) acceleration error for $N = 10^7$ particles drawn from a Plummer sphere. The top panel reports runs using multipole-acceptance criterion (16a) with a low-order-FMM estimate for a_b , while the bottom panel reports runs using multipole-acceptance criterion (16b) with a low-order-FMM estimate for f_b . Each pair of open and filled symbols (of same colour and ordinate) refers to another FMM run with expansion order p as indicated and a different value for parameter ϵ in equations (16). The timings include all phases of the computation, including tree building and low-order estimation of a_b or f_b —for comparison, the direct-summation calculation for obtaining the ‘true’ accelerations took 25k seconds on the same hardware. The thin dotted and dashed lines are power laws with exponents -0.16 and -0.2 , respectively.

caption to Fig. 9, but also because estimating f is easier and faster than estimating \mathbf{a} . Of course, the estimation of \mathbf{a} can be easily avoided in practice by using the accelerations from the previous time step.

6.3 Accuracy versus parameter ϵ

In any practical application there is, of course, no possibility to check on the actual error, so it is important to test how well it is reflected by the parameter ϵ . As can be seen from Fig. 11, the rms value for the respective error ($\delta a/a$ if using criterion 16a and $\delta a/f$ if using criterion 16b) is typically slightly less than ϵ for the optimal expansion order p . At intermediate values ($\epsilon \sim 10^{-8}$) the error is actually a factor ~ 2 smaller. The 99.99 percentile of the errors is typically a factor ten larger.

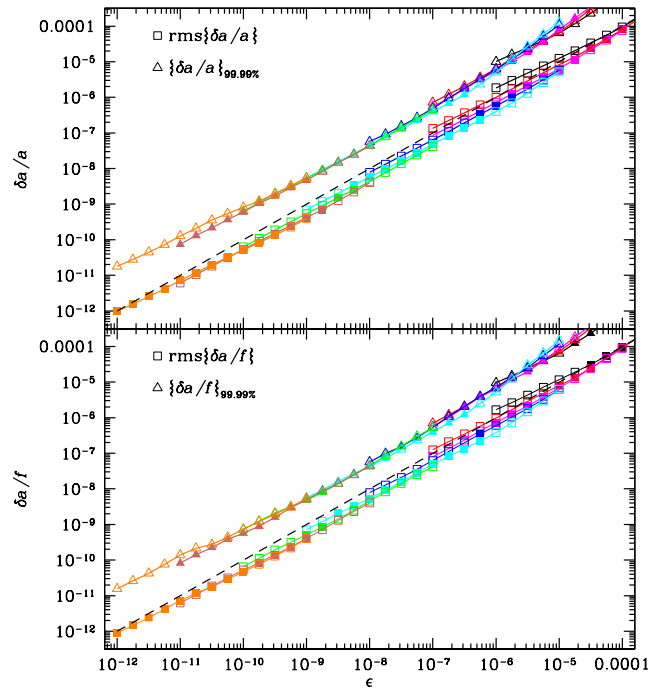


Fig. 11 Rms value (squares) or 99.99 percentile (triangles) of the error $\delta a/a$ (top) or $\delta a/f$ (bottom) versus parameter ϵ for the same runs as in Fig. 10 (using the same colour coding). Full symbols indicate that the expansion order is optimal, i.e. obtained minimal wall-clock time for the given error measure (lowest line in Fig. 10).

Table 2 Timings and errors as function of particle number N for FMM runs with $p = 10$, $\epsilon = 10^{-6.25}$, and using multipole-acceptance criterion (16b). The timings are given in seconds and refer to, respectively, the tree building; the estimation of f via low-order FMM; the passing up of \mathbf{z} , \mathbf{s} , $\min\{f\}$, and \mathcal{M}_n^m ; the dual tree walk; and the passing down of \mathcal{F}_n^m and evaluation of gravity. See also Fig. 12.

N	t_{tree}	t_{ffmm}	t_{up}	t_{walk}	t_{down}	$\{\delta a/f\}_{\text{rms}}$	$\{\delta a/f\}_{99.99\%}$
10^4	0.0004	0.0011	0.0012	0.0317	0.0005	2.81×10^{-7}	1.32×10^{-6}
10^5	0.0019	0.0042	0.0097	0.2131	0.0044	3.61×10^{-7}	2.51×10^{-6}
10^6	0.0290	0.0245	0.0957	1.5366	0.0431	3.85×10^{-7}	3.32×10^{-6}
10^7	0.2559	0.1897	0.8870	11.358	0.3999	4.05×10^{-7}	2.20×10^{-6}

6.4 Complexity: scaling with the number N of particles

The overall cost of my high-accuracy FMM implementation is dominated by the computation of all node-node interactions during the dual tree walk. All other phases (establishing the hierarchical tree structure, computing \mathbf{z} , \mathbf{s} , and \mathcal{M}_n^m for each cell; passing down \mathcal{F}_n^m and evaluating gravity for each sink position) contribute much less (see Tab. 2). When using a simple geometric multipole-acceptance criterion, such as equation (5), the FMM is well known to have complexity $\mathcal{O}(N)$ (e.g. Cheng et al, 1999). This is because distant interactions contribute less than $\mathcal{O}(N)$, so that the overall costs are dominated by the local interactions only (Dehnen, 2002).

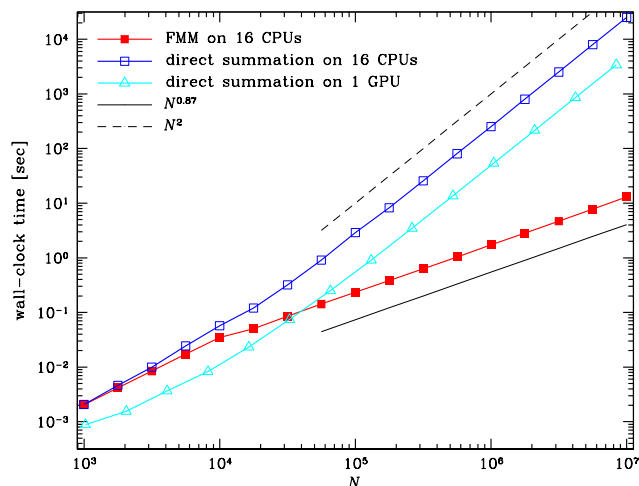


Fig. 12 Wall clock time for the computation of the mutual gravitational forces between N particles drawn from a Plummer sphere. The FMM (full squares) is parameterised (see Table 2) to yield acceleration errors very similar to those of direct summation on GPUs using the *sapporo* library (open triangles, using a NVIDIA K20M GPU accelerator)⁶. The direct summation on 16 CPUs (open squares) uses double precision and besides the accelerations also computes the gravitational potential and the scale f (equation 4).

I am not aware of theoretical estimates for the complexity for the case of more sophisticated multipole-acceptance criteria, but Dehnen (2002) reports an empirical scaling proportional to $N^{0.93}$ for his approach of a mass-dependent opening angle. Table 2 and Fig. 12 present the timings obtained with my implementation using $p = 10$, $\epsilon = 10^{-6.25}$, and low-order FMM estimates of f_b in equation (16b). With these settings, the acceleration errors are comparable to those generated via the *sapporo* library on a GPU (the current state-of-the-art force solver for collisional N -body simulations), as reported in Section 3.2.

From Table 2, it can be seen that the costs for tree building grow faster than linearly with N ($N \ln N$ is expected), those for the upward and downward passes roughly linearly with N (as expected), but those for the FMM estimation of f and the dual tree walk less than linearly. As a result, the total computational costs are very well fit by the power law $N^{0.87}$ for $N > 10^4$, see Fig. 12.

This Figure also shows the timings for a (double-precision) direct-summation on the same hardware (yielding much more accurate accelerations) and for a mixed-precision direct-summation on a GPU using the *sapporo* library (yielding comparably accurate accelerations)⁶. At large (but realistic) N FMM out-performs direct summation, even if accelerated using a GPU.

⁶ The timings for the *sapporo* library also include additional computations (nearest neighbour finding and neighbour listing). These contribute negligibly at large N , but at small N they are, together with latency on the GPU, responsible for the deviation of the observed complexity from N^2 .

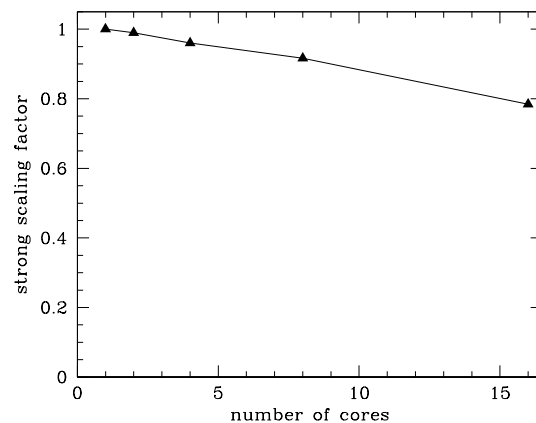


Fig. 13 Strong scaling of my implementation for the computation of the mutual forces for $N = 10^7$ particles with $p = 10$ and $\epsilon = 10^{-6.25}$.

6.5 Scaling with the number of CPUs

Fig. 13 plots the strong scaling factor t_1/nt_n for my multi-threaded implementation. The scaling drops to 80% for 16 cores, which is not untypical for multi-threaded programs. This drop is presumably caused by imbalances at synchronisation points, of which the implementation has many. Most of these are not algorithmically required, but allow for a much easier implementation. Clearly, any massively parallel implementation needs to address this issue to retain good scaling for large numbers of processors.

7 Beyond simple gravity approximation

So far, I have considered the approximate computation of the unsoftened gravitational potential and acceleration at all particle positions with equal relative (or scaled) accuracy. However, the fast multipole method can be easily modified or extended beyond that.

For example, one may want to have individual accuracy parameters ϵ_b instead of a global one. This is easily accommodated by replacing $\epsilon \min_{b \in B} \{a_b\}$ in criterion (16a) with $\min_{b \in B} \{\epsilon_b a_b\}$ and analogously for criterion (16b).

When using individual ϵ_b , but also in general, it may be beneficial to adapt the expansion order p to the accuracy actually required for a given cell \rightarrow cell interaction. This could be implemented by using the lowest $p \leq p_{\max}$ for which the multipole-acceptance criterion is satisfied.

7.1 Force computation for a subset of particles

Most N -body codes employ adaptive individual time steps for each particle. The standard technique is Makino's (1991) block-step scheme, where the forces of all *active* particles are computed synchronously. Active are those particles with

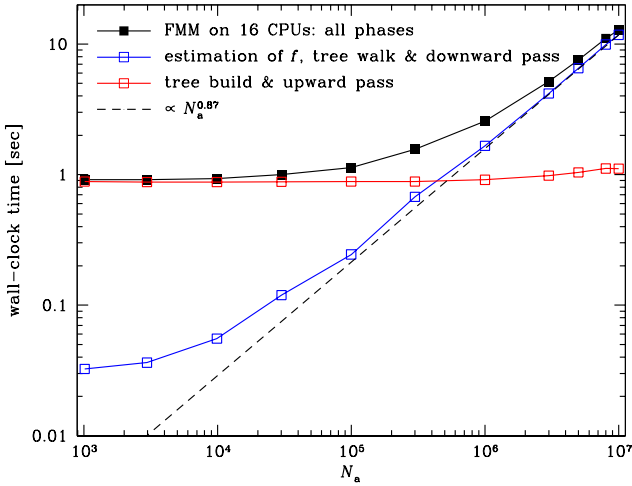


Fig. 14 Wall clock time for the computation of gravity for the innermost N_a of $N = 10^7$ particles (of a Plummer sphere), using the same parameters (p and ε) as in Fig. 12.

time step smaller than some threshold (which varies from one force computation to the next).

When using FMM in such a situation, only interactions with sink cells contain at least one active particle must be considered. If the fraction of active particles in such cells is small (but non-zero), FMM becomes much less efficient per force computation. Fortunately, however, active particles are typically spatially correlated (because the time steps of adjacent particles are similar), such that the fraction of active particles is either zero or large.

I performed some practical tests, where only particles within some distance from the origin of the system were considered active. Fig. 14 plots the wall-clock time vs. the number N_a of active particles for $N = 10^7$. As expected the costs for the preparation phase (tree building and upward pass) are largely independent of N_a (the slight increase of the red curve at large N_a is because \mathbf{s} and ρ_s are computed as part of the upward pass, but only for cells with active particles).

The costs for the interaction and downward pass, on the other hand, decrease roughly like $N_a^{0.87}$ for $N_a \gtrsim 10^4$. The net effect is that for $N_a/N \lesssim 0.01$, the costs are almost completely dominated by the preparation phase, and hence independent of N_a . The precise point of this transition depends on N and the FMM parameters. For smaller N and/or more accurate forces, the relative contribution of the tree-walk phase increases and the transition occurs at smaller N_a .

There is certainly some room for improvement by, e.g. using a smaller expansion order p than is optimal for $N_a = N$ and/or re-cycling the tree structure from the previous time step. Both measures reduce the costs of the preparation phase and increase that of the interaction phase (at given ε), but shall reduce the overall costs if $N_a \ll N$.

7.2 Softened gravity or far-field force

Gravitational softening amounts to replacing the Newtonian Greens function $\psi = |\mathbf{r}|^{-1}$ by (Dehnen, 2001)

$$\psi(\mathbf{r}) = h^{-1} \varphi(|\mathbf{r}|/h) \quad (17)$$

with softening length h and *softening kernel* $\varphi(q) \rightarrow q^{-1}$ as $q \rightarrow \infty$. This corresponds to replacing each source point by a smooth mass distribution with density $\mu_b \rho(\mathbf{x} - \mathbf{x}_b)$, where

$$\rho(\mathbf{r}) = -(4\pi)^{-1} \nabla^2 \psi(\mathbf{r}). \quad (18)$$

This Greens function (17) is no longer harmonic and harmonic FMM cannot be used. One obvious option is to use the more general Cartesian FMM of Appendix A.1 (Dehnen, 2002). The computational costs of this approach grow faster with expansion order p , such that small approximation errors (requiring high p) become significantly more expensive. However, small approximation errors are hardly required in situations where gravitational softening is employed. Alternatively, if softening is restricted to a finite region, i.e. if $\rho(\mathbf{r}) = 0$ for $|\mathbf{r}| \geq h$, harmonic FMM can still be used to compute gravity from all sources at distances $|\mathbf{r}| \geq h$, while direct summation could be used for *neighbours*, sources at $|\mathbf{r}| < h$. This approach is sensible only if the number of neighbours is sufficiently bounded (so that the cost incurred by the direction summation remains small). This is the case, in particular, if the number of neighbours is kept (nearly) constant by adapting the individual softening lengths h_i in order to adapt the numerical resolution (Price and Monaghan, 2007).

In practice, this requires to carry with each cell the radius $h_{\mathbf{z}} > \rho_{\mathbf{z}}$ of the smallest sphere centred on \mathbf{z} which contains all softening spheres of its sources, and allow a FMM interaction $A \rightarrow B$ only if $|\mathbf{z}_A - \mathbf{s}_B| > h_{\mathbf{z}_A} + \rho_{\mathbf{s}_B}$.

The same technique can be used to restrict the FMM approximation to the far field for each particle, i.e. the force generated by all sources outside of a sphere of known radius h_b around \mathbf{x}_b .

7.3 Jerk, snap, crackle, and pop

The jerk is the total time derivative of the acceleration

$$\mathbf{j} = \dot{\mathbf{a}} = \frac{d}{dt} \frac{\partial \Psi}{\partial \mathbf{x}}. \quad (19)$$

The simplest way to estimate this using FMM, is to not allow the expansion centres to have any velocity ($\dot{\mathbf{z}} = \dot{\mathbf{s}} = 0$), such

that differentiating the FMM relations (3) w.r.t. time gives

$$\dot{\Psi}_n^m(\mathbf{x}_b) = \sum_{k=0}^{p-n} \sum_{l=-k}^k \left[\dot{Y}_k^{l*}(\mathbf{s}_B - \mathbf{x}_b) \mathcal{F}_{n+k}^{m+l}(\mathbf{s}_B) + \dot{Y}_k^{l*}(\mathbf{s}_B - \mathbf{x}_b, -\dot{\mathbf{x}}_b) \mathcal{F}_{n+k}^{m+l}(\mathbf{s}_B) \right] + \delta \dot{\Psi}_n^m, \quad (20a)$$

$$\dot{\mathcal{F}}_n^m(\mathbf{s}_B) = \sum_{k=0}^{p-n} \sum_{l=-k}^k \dot{\mathcal{M}}_k^{l*}(\mathbf{z}_A) \Theta_{n+k}^{m+l}(\mathbf{s}_B - \mathbf{z}_A), \quad (20b)$$

$$\dot{\mathcal{M}}_n^m(\mathbf{z}_A) = \sum_{a \in A} \mu_a \dot{Y}_n^m(\mathbf{x}_a - \mathbf{z}_A, \dot{\mathbf{x}}_a). \quad (20c)$$

and the jerk follows from $\mathbf{j} = -(\Re\{\dot{\Psi}_1^1\}, \Im\{\dot{\Psi}_1^1\}, \dot{\Psi}_1^0)$. Since $\dot{\mathbf{z}} = \dot{\mathbf{s}} = 0$, the M2M and L2L kernels (equations 3d and 3e) work also for the time derivatives $\dot{\mathcal{M}}_n^m$ and $\dot{\mathcal{F}}_n^m$ of the multipoles and field tensors, respectively. The relations for the next order, the snap $\mathbf{s} = \dot{\mathbf{a}}$, can be derived by differentiating yet again.

With each additional order (jerk, snap, crackle, pop, ...), the computational cost of the combined M2L kernels is not more than the corresponding multiple of the ordinary M2L kernel (i.e. acceleration plus jerk are twice as costly as just acceleration). This is a direct consequence of not allowing cell-centre velocities hence preventing the terms depending on \mathbf{z} or \mathbf{s} in equations (3) to carry any time dependence. In contrast, the computational costs of the P2M and L2P kernels grows quadratically with the order of time derivative. This is not really a problem, since those kernels are only needed once per particle, while the M2L kernel is typically used $\gtrsim 100$ times more often.

7.4 The tidal field

FMM can also be used to approximate the Hessian

$$\mathbb{T}_b = \nabla \nabla \Psi(\mathbf{x}_b) \quad (21)$$

of the potential, which is given by the components of Ψ_2^m via

$$\begin{aligned} T_{xx} &= -\frac{1}{2} \Psi_2^0 + \frac{1}{2} \Re\{\Psi_2^2\}, \\ T_{xy} &= -\frac{1}{2} \Im\{\Psi_2^2\}, \\ T_{xz} &= \Re\{\Psi_2^1\}, \\ T_{yy} &= -\frac{1}{2} \Psi_2^0 - \frac{1}{2} \Re\{\Psi_2^2\}, \\ T_{yz} &= \Im\{\Psi_2^1\}, \quad \text{and} \\ T_{zz} &= \Psi_2^0 \end{aligned} \quad (22)$$

(in particular $\text{tr}(\mathbb{T}) = 0$ as expected). Note, however, that the accuracy of this approximation is lower than that for the acceleration. \mathbb{T} is of particular interest in collisionless N -body modelling, when

$$\tau_b \leq \eta \|\mathbb{T}_b\|^{-1/4} \quad (23)$$

with dimensionless parameter $\eta \ll 1$ has been suggested as criterion for individual particle time steps (Dehnen and

Read, 2011). The matrix norm of \mathbb{T} may be directly computed from Ψ_2^m as

$$\|\mathbb{T}_b\| = \frac{3}{2} |\Psi_2^0|^2 + 2 |\Psi_2^1|^2 + \frac{1}{2} |\Psi_2^2|^2. \quad (24)$$

8 Discussion and Conclusions

The fast multipole method (FMM) approximates the computation of the mutual forces between N particles. I have derived the relevant mathematical background, giving much simpler formulæ than the existing literature, for the case of unsoftened gravity, when the harmony of the Greens function allows significant reduction of the computational complexity.

Like the tree code, my FMM implementation uses a hierarchical tree of spatial cells. Unlike the tree code, FMM uses cell \rightarrow cell interactions, which account for all interactions between sources in the first cell and sinks in the second. Almost all distant particle \rightarrow particle interactions are ‘caught’ by fewer than $\mathcal{O}(N)$ cell \rightarrow cell interactions, such that local interactions, requiring $\mathcal{O}(N)$ computations, dominate the overall workload (Dehnen, 2002). With the tree code, the situation is reversed: the distant interactions require $\mathcal{O}(N \ln N)$ computations and dominate the overall work. This implies that FMM has the best complexity of all known force solvers. What is more, the predominance of local as opposed to distant interactions makes FMM ideally suited for applications on super-computers, where communications (required by distant interactions) are increasingly more costly than computations. However, FMM is inherently difficult to parallelise and this study considered only a multi-threaded implementation with a task-parallel dual tree walk (the core of FMM).

Most previous implementations of FMM considered simple choices for the cell’s multipole- and force-expansion centres and the multipole-acceptance criterion which decides whether a given cell \rightarrow cell interaction shall be processed via the multipole expansion or be split into daughter interactions. Traditionally, a simple opening-angle based multipole-acceptance criterion has been used and cell centres equal to either the cell’s geometric centre or its centre of mass. These choices, which presumably were based on computational convenience and intuition, inevitably result in a wide distribution of individual relative force errors with extended tails reaching ~ 1000 times the median.

The main goal of this study was avoid such extended tails of large force errors and to minimise the computational effort at a given force accuracy. The key for achieving this goal is a reasonably accurate estimate, based on the multipole power of the source cell and the size of the sink cell, for the actual force error incurred by individual cell \rightarrow cell interactions. Based on the insight from this estimate, I set the cell’s force-expansion centres to (an approximation of) the centre of the smallest sphere enclosing all its particles,

when the cell size and hence the error estimates are minimal. I also use the new estimates in the multipole-acceptance criterion, such that each cell \rightarrow cell interaction is considered on the merit of the error it likely incurs. This results in very well behaved distributions of the relative force errors, provided an initial estimate for the forces is at hand. This can either be taken from the previous time step or obtained via low-accuracy FMM.

After these improvements, the method has only two free parameters: the expansion order p and a parameter ε for the relative force error. Experiments showed that the actual rms relative force error is typically somewhat less than ε , while for any given ε there is an optimum p at which the computational cost are minimal. For $\varepsilon = 10^{-6.25}$, for example, $p = 10$ is optimal and the accelerations errors are comparable to those of direct summation on a GPU (the current state-of-the-art method for collisional N -body simulations). With these parameter settings, the computational costs scale like $N^{0.87}$ for large N and the method out-performs any direct-summation implementation for $N \gtrsim 10^5$. When computing only the forces for $N_a < N$ of N particles, the costs are roughly proportional to $N_a^{0.87}$ for $N_a/N \gtrsim 0.01$, but become independent of N_a below that (where the costs for tree building dominate). For large N , this is still significantly faster than direct summation.

An implementation of the FMM on a GPU accelerator should yield a further significant speed-up compared to my CPU-based implementation, though this is certainly a challenging task, given that FMM is algorithmically more complex than direct summation or a tree code (both of which have been successfully ported to the GPU). Presumably a somewhat lesser challenge is a massively parallel implementation of the method, which can be run on a super computer.

A practical application of FMM in an actual collisional N -body simulation would be very interesting. Since the force between close neighbours is always computed directly (in double precision) as explained earlier, close encounters can be treated essentially in the same fashion as with existing techniques. However, an unfortunate hindrance to an application of the presented techniques originates from the long marriage of existing collisional N -body techniques with direct summation. Methods, such as the Ahmad-Cohen neighbour scheme, to reduce the need for the costly far-field force summations are not necessary with FMM, and the existing N -body tools are not well suited for an immediate application of FMM.

Acknowledgements The author thanks Joachim Stadel for many helpful discussions and the suggestion to allow $\mathbf{z} \neq \mathbf{s}$, Alessia Gualandris for running sapporo to provide the data for Fig. 3, and Simon Portegies Zwart and Jeroen Bédorf for providing the timings for sapporo 2 in Fig. 12. This work was supported by STFC consolidated grant ST/K001000/1.

References

- Ahmad A, Cohen L (1973) A numerical integration scheme for the N -body gravitational problem. *J Comp Phys* 12:389–402, DOI 10.1016/0021-9991(73)90160-5
- Applequist J (1989) Traceless cartesian tensor forms for spherical harmonic functions: new theorems and applications to electrostatics of dielectric media. *Journal of Physics A Mathematical General* 22:4303–4330, DOI 10.1088/0305-4470/22/20/011
- Barnes J, Hut P (1986) A Hierarchical $O(N \log N)$ Force-Calculation Algorithm. *Nature* 324:446–449
- Capuzzo-Dolcetta R, Miocchi P (1998) A comparison between the fast multipole algorithm and the tree-code to evaluate gravitational forces in 3-D. *J Comp Phys* 143:29–48, DOI 10.1006/jcph.1998.5949, astro-ph/9703122
- Cheng H, Greengard L, Rokhlin V (1999) A Fast Adaptive Multipole Algorithm in Three Dimensions. *J Comp Phys* 155:468–498, DOI 10.1006/jcph.1999.6355
- Dehnen W (2000) A Very Fast and Momentum-conserving Tree Code. *ApJ* 536:L39–L42
- Dehnen W (2001) Towards optimal softening in three-dimensional N -body codes - I. Minimizing the force error. *MNRAS* 324:273–291
- Dehnen W (2002) A Hierarchical $O(N)$ Force Calculation Algorithm. *J Comp Phys* 179:27–42
- Dehnen W, Read JI (2011) N -body simulations of gravitational dynamics. *European Physical Journal Plus* 126:55, DOI 10.1140/epjp/i2011-11055-3
- Fischer K, Gärtner B, Herrmann T, Hoffmann M, Schönherr S (2013) Bounding volumes. In: *CGAL User and Reference Manual*, 4.2 edn, CGAL Editorial Board, <http://www.cgal.org/Manual/4.2>
- Gaburov E, Harfst S, Portegies Zwart S (2009) SAPPORO: A way to turn your graphics cards into a GRAPE-6. *New Astronomy* 14(7):630–637, DOI <http://dx.doi.org/10.1016/j.newast.2009.03.002>
- Gradshteyn IS, Ryzhik I (1994) *Table of Integrals, Series, and Products*, 5th edn. London, Academic Press
- Greengard L, Rokhlin V (1987) A fast algorithm for particle simulations. *J Comp Phys* 73:325–348, DOI 10.1016/0021-9991(87)90140-9
- Hinsen K, Felderhof BU (1992) Reduced description of electric multipole potential in Cartesian coordinates. *J Math Phys* 33:3731–3735
- Hobson EW (1931) *The theory of spherical and ellipsoidal harmonics*. Cambridge, Cambridge University Press
- James RW (1969) Transformation of Spherical Harmonics Under Change of Reference Frame. *Geophys J Intnl* 17:305–316
- Makino J (1991) Optimal order and time-step criterion for Aarseth-type N -body integrators. *ApJ* 369:200–212, DOI 10.1086/169751
- Makino J, Taiji M (1998) *Scientific Simulations with Special-Purpose Computers—the GRAPE Systems*. Wiley
- Matoušek J, Sharir M, Welzl E (1996) A Subexponential Bound for Linear Programming. *Algorithmica* 16:498–516
- Maxwell JC (1892) *Treatise on Electricity and Magnetism*. Oxford, Oxford University Press
- Pinchon D, Hoggan PE (2007) Rotation matrices for real spherical harmonics: general rotations of atomic orbitals in space-fixed axes. *J Phys A: Math Theor* 40:1597–1610, DOI 10.1088/1751-8113/40/7/011
- Plummer HC (1911) On the problem of distribution in globular star clusters. *MNRAS* 71:460–470
- Price DJ, Monaghan JJ (2007) An energy-conserving formalism for adaptive gravitational force softening in smoothed particle hydrodynamics and N -body codes. *MNRAS* 374:1347–1358, DOI 10.1111/j.1365-2966.2006.11241.x
- Reinders J (2007) *Intel Threading Building Blocks*. O'Reilly Media, Sebastopol

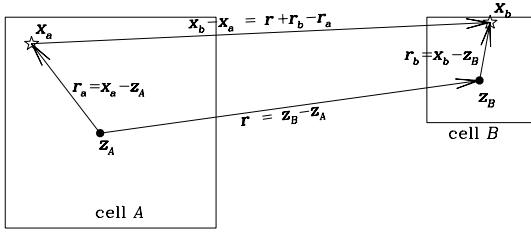


Fig. 15 The Greens function for the interaction between particles a and b at positions \mathbf{x}_a and \mathbf{x}_b and residing in cells A and B , is approximated by Taylor expanding the Greens function about \mathbf{r} , the distance vector between the cell centres \mathbf{z}_A and \mathbf{z}_B .

Salmon JK, Warren MS (1994) Skeletons from the treecode closet. *J Comp Phys* 111:136–155, DOI 10.1006/jcph.1994.1050
 Taura K, Nakashima J, Yokota R, Maruyama N (2012) A Task Parallel Implementation of Fast Multipole Methods. *High Performance Computing, Networking Storage and Analysis, SC Companion: 0:617–625*, <http://doi.ieeecomputersociety.org/10.1109/SC.Companion.2012.86>

A Derivation of the FMM relations

Here, the FMM relations given in Section 2 are derived and motivated. Differently from the main text, the multipole and force expansion centres, \mathbf{z} and \mathbf{s} , are not explicitly distinguished and instead \mathbf{z} is used for either. The general case $\mathbf{z} \neq \mathbf{s}$ is a trivial generalisation.

A.1 Cartesian FMM

The distance vector $\mathbf{x}_b - \mathbf{x}_a$ between two particles residing in two well-separated cells A and B , respectively, can be decomposed into three components (see also Fig. 15)

$$\mathbf{x}_b - \mathbf{x}_a = \mathbf{r} + \mathbf{r}_b - \mathbf{r}_a \quad (25)$$

with $\mathbf{r}_a \equiv \mathbf{x}_a - \mathbf{z}_A$, $\mathbf{r}_b \equiv \mathbf{x}_b - \mathbf{z}_B$, and $\mathbf{r} \equiv \mathbf{z}_B - \mathbf{z}_A$. The Taylor expansion of the general Greens function $\psi(\mathbf{x}_b - \mathbf{x}_a)$ in \mathbf{r}_a and \mathbf{r}_b up to order p then reads⁷

$$\psi(\mathbf{x}_b - \mathbf{x}_a) = \sum_{|\mathbf{n}|=0}^p \sum_{|\mathbf{m}|=0}^{p-|\mathbf{n}|} \frac{(-1)^{|\mathbf{m}|}}{\mathbf{n}!\mathbf{m}!} \mathbf{r}_b^{\mathbf{n}} \mathbf{r}_a^{\mathbf{m}} \nabla^{\mathbf{n}+\mathbf{m}} \psi(\mathbf{r}) + \mathcal{R}_p. \quad (26)$$

This series converges (the remainder $\mathcal{R}_p \rightarrow 0$) as $p \rightarrow \infty$, if $|\mathbf{r}_a + \mathbf{r}_b| < |\mathbf{r}|$. Inserting (26) into the expression

$$\Psi_{A \rightarrow B}(\mathbf{x}_b) = \sum_{a \in A} \mu_a \psi(\mathbf{x}_b - \mathbf{x}_a) \quad (27)$$

for the (negative) potential due to all source points in cell A and for any sink position \mathbf{x}_b in cell B , one obtains after re-arranging

$$\Psi_{A \rightarrow B}(\mathbf{x}_b) = \sum_{|\mathbf{n}|=0}^p \frac{1}{\mathbf{n}!} (\mathbf{x}_b - \mathbf{z}_B)^{\mathbf{n}} \mathbf{F}_{\mathbf{n}}(\mathbf{z}_B) + \delta \Psi_{A \rightarrow B}, \quad (28a)$$

$$\mathbf{F}_{\mathbf{n}}(\mathbf{z}_B) \equiv \sum_{|\mathbf{m}|=0}^{p-|\mathbf{n}|} \mathbf{M}_{\mathbf{m}}(\mathbf{z}_A) \mathbf{D}_{\mathbf{n}+\mathbf{m}}(\mathbf{z}_B - \mathbf{z}_A), \quad (28b)$$

$$\mathbf{M}_{\mathbf{m}}(\mathbf{z}_A) \equiv \sum_{a \in A} \mu_a \frac{(-1)^{|\mathbf{m}|}}{\mathbf{m}!} (\mathbf{x}_a - \mathbf{z}_A)^{\mathbf{m}} \quad (28c)$$

⁷ Using *multi-index* notation $\mathbf{n} \equiv (n_x, n_y, n_z)$ with $n \equiv |\mathbf{n}| \equiv n_x + n_y + n_z$, such that the first sum in (26) is over non-negative integer triples \mathbf{n} with $n_x + n_y + n_z \leq p$. Furthermore $\mathbf{n}! \equiv n_x! n_y! n_z!$ and $\mathbf{r}^{\mathbf{n}} \equiv r_x^{n_x} r_y^{n_y} r_z^{n_z}$.

with the derivatives $\mathbf{D}_{\mathbf{n}}(\mathbf{r}) \equiv \nabla^{\mathbf{n}} \psi(\mathbf{r})$. The FMM algorithm essentially works these equations backwards: in a first step, the *multipoles* $\mathbf{M}_{\mathbf{m}}(\mathbf{z})$ are computed for each cell via (28c) and by utilising those of daughter cells via the shifting formula

$$\mathbf{M}_{\mathbf{m}}(\mathbf{z} + \mathbf{x}) = \sum_{\mathbf{n}=0}^{\mathbf{m}} \frac{\mathbf{x}^{\mathbf{n}}}{\mathbf{n}!} \mathbf{M}_{\mathbf{m}-\mathbf{n}}(\mathbf{z}). \quad (28d)$$

Second, for each cell the *field tensors* $\mathbf{F}_{\mathbf{n}}(\mathbf{z})$ of all its interactions are computed via (28b) and added up. Finally, the field tensors are passed down the tree, utilising the shifting formula

$$\mathbf{F}_{\mathbf{n}}(\mathbf{z} + \mathbf{x}) = \sum_{|\mathbf{m}|=0}^{p-|\mathbf{n}|} \frac{\mathbf{x}^{\mathbf{m}}}{\mathbf{m}!} \mathbf{F}_{\mathbf{n}+\mathbf{m}}(\mathbf{z}), \quad (28e)$$

and the potential (and its derivative, the acceleration) is evaluated via (28a) at each sink position. Equations (28) are the basis of Cartesian FMM, such as implemented in Dehnen's (2000; 2002) *falcON* algorithm.

At each order $n = |\mathbf{n}|$, there are $\binom{n+2}{2}$ coefficients $\mathbf{F}_{\mathbf{n}}$ (as well as $\mathbf{M}_{\mathbf{n}}$ and $\mathbf{D}_{\mathbf{n}}$), and the total number of coefficients up to order p is $\binom{p+3}{3}$. The computational effort of the resulting algorithm is dominated by their computation in (28b), which requires about $\binom{p+6}{6}$ multiplications. Thus at large p a straightforward application of this method approaches an operation count of $\mathcal{O}(p^6)$. The computation (28b) of the field tensors is essentially a convolution in index space and hence can be accelerated using a fast Fourier technique with costs $\mathcal{O}(p^3 \ln p)$ (but see footnote 2).

A.2 Harmonic tensors

For the important case $\psi = |\mathbf{r}|^{-1}$ corresponding to gravitational and electrostatic forces, the above method can be improved by exploiting that this Greens function is *harmonic*, i.e. $\nabla^2 \psi = 0$ for $|\mathbf{r}| > 0$. As a consequence, the $\mathbf{D}_{\mathbf{n}} = \nabla^{\mathbf{n}} \psi$ are harmonic too and satisfy

$$\nabla^2 \mathbf{D}_{\mathbf{k}} = \mathbf{D}_{\mathbf{k}+(2,0,0)} + \mathbf{D}_{\mathbf{k}+(0,2,0)} + \mathbf{D}_{\mathbf{k}+(0,0,2)} = 0. \quad (29)$$

In other words: $\mathbf{D}_{\mathbf{n}}$ is *traceless*. At given degree $n = k+2$, equation (29) gives $\binom{n}{2}$ constraints such that of the $\binom{n+2}{2}$ terms only $2n+1$ are truly independent. In inner products, a traceless tensor only ‘sees’ the traceless part of its co-operand:

$$\sum_{|\mathbf{n}|=n} \bar{\mathbf{A}}_{\mathbf{n}} \mathbf{B}_{\mathbf{n}} = \sum_{|\mathbf{n}|=n} \bar{\mathbf{A}}_{\mathbf{n}} \bar{\mathbf{B}}_{\mathbf{n}} = \sum_{|\mathbf{n}|=n} \mathbf{A}_{\mathbf{n}} \bar{\mathbf{B}}_{\mathbf{n}}, \quad (30)$$

where the ‘reduced’ tensor $\bar{\mathbf{A}}_{\mathbf{n}}$ denotes the traceless part of $\mathbf{A}_{\mathbf{n}}$. Furthermore, $\bar{\mathbf{r}}^{\mathbf{n}}$ is related to $\mathbf{D}_{\mathbf{n}}$ via

$$\mathbf{D}_{\mathbf{n}}(\mathbf{r}) = (-1)^n (2n-1)!! \frac{\bar{\mathbf{r}}^{\mathbf{n}}}{r^{2n+1}}. \quad (31)$$

With these relations, the Taylor series of the harmonic Greens function becomes, for $r > x$

$$\frac{1}{|\mathbf{r} - \mathbf{x}|} = \sum_{n=0}^{\infty} \frac{x^n}{r^{n+1}} \sum_{|\mathbf{n}|=n} \frac{(2n-1)!!}{\mathbf{n}!} \frac{\bar{\mathbf{x}}^{\mathbf{n}} \bar{\mathbf{r}}^{\mathbf{n}}}{r^n}, \quad (32)$$

which is the Cartesian equivalent to the spherical harmonic expansion

$$\frac{1}{|\mathbf{r} - \mathbf{x}|} = \sum_{n=0}^{\infty} \frac{x^n}{r^{n+1}} \sum_{m=-n}^n Y_n^m(\hat{\mathbf{x}}) Y_n^{m*}(\hat{\mathbf{r}}) \quad (33)$$

(see eq. (42) for a definition of Y_n^m). While at each order n there are only $2n+1$ truly independent terms, the expansion (32) still carries all $\binom{n+2}{2}$ terms, amounting to a total of $\binom{p+3}{3}$ terms in an expansion up to order p . The equivalent spherical harmonic expansion (33) only carries $2n+1$ terms per order⁸ amounting to a total of $(p+1)^2$, i.e. at large p is much preferable.

⁸ In equation (33), the Y_l^m are complex-valued for $m \neq 0$, but because of their symmetry $Y_l^{m*} = (-1)^m Y_l^{-m}$ there are only $2n+1$ independent real-valued components per order n .

The number of terms actually used can be reduced to $(2n+1)$ per order, for example, by omitting all terms with $n_z > 1$ and recover their contribution via recursive application of

$$D_{\mathbf{k}+(0,0,2)} = -D_{\mathbf{k}+(2,0,0)} - D_{\mathbf{k}+(0,2,0)} \quad (34)$$

(Applequist, 1989; Hinsen and Felderhof, 1992). However, the resulting algebraic challenges are considerable, though the overall computational effort could well be reduced to $\mathcal{O}(p^3)$ operations (Joachim Stadel, private communication), but I am not aware of a systematic demonstration.

A.3 Spherical harmonics

The algebraic complications with obtaining an efficient Cartesian FMM stem from the fact that the Laplace operator involves three terms, such that the resulting recovery relation (34) has two terms instead of one on the right-hand side. This problem can be avoided by Taylor expanding in other than Cartesian coordinates where the Laplace operator involves only two instead of three terms.

The simplest possibility is a linear combination of Cartesian coordinates with complex coefficients. The standard FMM relations emerge from replacing x and y with

$$\xi \equiv \frac{1}{2}(x+iy) \quad \text{and} \quad \eta \equiv -\frac{1}{2}(x-iy) = -\xi^*, \quad (35)$$

while keeping z . Then $\partial_\xi = \partial_x - i\partial_y$ and $\partial_\eta = -\partial_x - i\partial_y$, such that $\partial_\xi^2 + \partial_\eta^2 = -\partial_x^2 - \partial_y^2$ and hence for harmonic functions

$$\partial_\xi \partial_\eta = \partial_z^2, \quad (36)$$

or $D_{\mathbf{k}+(0,0,2)} = D_{\mathbf{k}+(1,1,0)}$ in place of equation (34). With this relation one can eliminate all mixed ξ - η derivatives in favour of z derivatives. This in turn allows a reduction in the number of indices from three to two by using the total number n of derivatives and the number $|m|$ of ξ (for $m < 0$) or η derivatives (for $m > 0$).

Somewhat surprisingly, the relations required for FMM are hardly covered by the rich literature on spherical harmonics (and FMM). To derive the relevant formulae, I follow the ideas of Maxwell (1892, see also James 1969) and define the differential operator

$$\Delta_n^m \equiv \begin{cases} (-\partial_z)^{n-|m|} \partial_\xi^{|m|} & -n \leq m < 0, \\ (-\partial_z)^{n-|m|} \partial_\eta^{|m|} & 0 \leq m \leq n, \\ 0 & |m| > n. \end{cases} \quad (37)$$

When applied to harmonic functions, this operator satisfies

$$\Delta_n^m \Delta_k^l = \Delta_{n+k}^{l+m}, \quad (38)$$

which can be shown via equation (36) and is inevitably linked to

$$\Delta_n^{-m} = (-1)^m \Delta_n^{m*}. \quad (39)$$

Since $\psi = |\mathbf{r}|^{-1}$ is harmonic, its derivatives

$$\Theta_n^m(\mathbf{r}) \equiv \Delta_n^m |\mathbf{r}|^{-1} \quad (40)$$

are harmonic too. Moreover, the functions $\Theta_n^m(\mathbf{r})$ are homogeneous of degree $-(n+1)$, i.e. $\Theta_n^m(\alpha\mathbf{r}) = \alpha^{-(n+1)}\Theta_n^m(\mathbf{r})$. I also define the *solid spherical harmonic* of degree n as

$$Y_n^m(\mathbf{r}) \equiv \frac{r^{-1} \Theta_n^m(\mathbf{r}/r^2)}{(n-m)!(n+m)!} = \frac{r^{2n+1} \Theta_n^m(\mathbf{r})}{(n-m)!(n+m)!}. \quad (41)$$

That Y_n^m is harmonic follows from the fact that if $f(\mathbf{r})$ is harmonic, then so is $r^{-1}f(\mathbf{r}/r^2)$ (Hobson, 1931, try this with your undergraduate students). Note that $Y_n^m(\mathbf{r})$ is just a homogeneous polynomial of total degree n in x , y and z . These harmonics are related to the usual normalised *surface spherical harmonic*

$$Y_n^m(\hat{\mathbf{r}}) \equiv (-1)^m \sqrt{\frac{(n-m)!}{(n+m)!}} P_n^m(\cos\theta) e^{im\phi} \quad (42)$$

via

$$\Theta_n^m(\mathbf{r}) = [(n-m)!(n+m)!]^{1/2} r^{-n-1} Y_n^m(\hat{\mathbf{r}}), \quad (43a)$$

$$Y_n^m(\mathbf{r}) = [(n-m)!(n+m)!]^{-1/2} r^n Y_n^m(\hat{\mathbf{r}}). \quad (43b)$$

Table 3 gives the first few harmonics in terms of x, y, z .

A.4 Spherical-harmonic FMM

In order to derive the relations for spherical-harmonic FMM, one must obtain the equivalent to the Cartesian Taylor expansion (26) and shift operations (28d,e). Via induction one can show that when applied to harmonic functions

$$\frac{1}{n!} (\mathbf{x} \cdot \nabla)^n = \sum_{m=-n}^n Y_n^{m*}(-\mathbf{x}) \Delta_n^m = \sum_{m=-n}^n Y_n^m(-\mathbf{x}) \Delta_n^{m*}, \quad (44)$$

which gives the translation operator for harmonic functions

$$\exp(\mathbf{x} \cdot \nabla) = \sum_{n=0}^{\infty} \sum_{m=-n}^n Y_n^m(-\mathbf{x}) \Delta_n^m = \sum_{n=0}^{\infty} \sum_{m=-n}^n Y_n^{m*}(-\mathbf{x}) \Delta_n^m. \quad (45)$$

When applying this to the harmonic Greens function, one gets

$$\frac{1}{|\mathbf{r}-\mathbf{x}|} = \sum_{n=0}^{\infty} \sum_{m=-n}^n Y_n^m(\mathbf{x}) \Theta_n^{m*}(\mathbf{r}), \quad (46)$$

which, because of equations (43), is equivalent to the standard form (33) and converges for $r > x$. Translating once again and employing (38) yields

$$\frac{1}{|\mathbf{r}-\mathbf{x}-\mathbf{y}|} = \sum_{k=0}^{\infty} \sum_{l=-k}^k \sum_{n=0}^{\infty} \sum_{m=-n}^n Y_n^m(\mathbf{x}) Y_k^l(\mathbf{y}) \Theta_{n+k}^{m+l*}(\mathbf{r}), \quad (47)$$

which converges for $r > |\mathbf{x} + \mathbf{y}|$. Comparing (46) and (47) one finds immediately the translation formula

$$Y_n^m(\mathbf{x} + \mathbf{y}) = \sum_{k=0}^n \sum_{l=-k}^k Y_k^l(\mathbf{x}) Y_{n-k}^{m-l}(\mathbf{y}). \quad (48)$$

When applying the translation operator (45) to Θ_n^m , one gets

$$\Theta_n^m(\mathbf{x} + \mathbf{y}) = \sum_{k=0}^{\infty} \sum_{l=-k}^k Y_k^{l*}(-\mathbf{y}) \Theta_{n+k}^{m+l}(\mathbf{x}). \quad (49)$$

As the Cartesian FMM relations (28) were based on equation (26), the spherical harmonic FMM relations (3) are based on equation (47), which for $\psi = |\mathbf{r}|^{-1}$ is completely equivalent but computationally more efficient.

A.5 Implementation details

A.5.1 Recursive evaluation of spherical harmonics

One may also obtain the relations

$$\Delta_k^l \Theta_n^m(\mathbf{x}) = \Theta_{n+k}^{m+l}(\mathbf{x}), \quad (50)$$

$$\Delta_k^l Y_n^m(\mathbf{x}) = (-1)^{k+l} Y_{n-k}^{m+l}(\mathbf{x}). \quad (51)$$

The first one follows immediately from equations (38) and (40), while the second can be deduced by equating (48) to $Y_n^m(\mathbf{x} + \mathbf{y})$ obtained by applying the translation operator (45). From these two relations combined with the operator relation (38) and the definitions (40) and (41), one can obtain numerous recurrence relations. For example, (omitting the arguments for brevity)

$$r^2 \Theta_n^m = (2n-1)z \Theta_{n-1}^m - ([n-1]^2 - m^2) \Theta_{n-2}^m, \quad (52)$$

$$(n^2 - m^2) Y_n^m = (2n-1)z Y_{n-1}^m - r^2 Y_{n-2}^m, \quad (53)$$

Table 3 The real-valued functions $(n-m)!(n+m)!U_n^m(\mathbf{r}) = r^{2n+1}T_n^m(\mathbf{r})$ for $n \leq 6$. See equations (58) for the relations to $Y_n^m(\mathbf{r})$ and $\Theta_n^m(\mathbf{r})$.

$m \setminus n$	0	1	2	3	4	5	6
6							$10395(x^6 - 15x^4y^2 + 15x^2y^4 - y^6)$
5						$945x(x^4 - 10x^2y^2 + 5y^4)$	$10395xz(x^4 - 10x^2y^2 + 5y^4)$
4					$105(x^4 - 6x^2y^2 + y^4)$	$945z(x^4 - 6x^2y^2 + y^4)$	$945(x^4 - 6x^2y^2 + y^4)(11z^2 - r^2)$
3				$15x(x^2 - 3y^2)$	$105xz(x^2 - 3y^2)$	$105x(x^2 - 3y^2)(9z^2 - r^2)$	$945xz(x^2 - 3y^2)(11z^2 - 3r^2)$
2			$3(x^2 - y^2)$	$15z(x^2 - y^2)$	$15(x^2 - y^2)(7z^2 - r^2)$	$315z(x^2 - y^2)(3z^2 - r^2)$	$315(x^2 - y^2)(33z^4 - 18z^2r^2 + r^4)$
1	x	$3xz$	$3x(5z^2 - r^2)$	$3x(5z^2 - r^2)$	$15xz(7z^2 - 3r^2)$	$45x(21z^4 - 14z^2r^2 + r^4)$	$315xz(33z^4 - 30z^2r^2 + 5r^4)$
0	1	z	$3z^2 - r^2$	$3z(5z^2 - 3r^2)$	$3(35z^4 - 30z^2r^2 + 3r^4)$	$15z(63z^4 - 70z^2r^2 + 15r^4)$	$45(231z^6 - 315z^4r^2 + 105z^2r^4 - 5r^6)$
-1		y	$3yz$	$3y(5z^2 - r^2)$	$15yz(7z^2 - 3r^2)$	$45y(21z^4 - 14z^2r^2 + r^4)$	$315yz(33z^4 - 30z^2r^2 + 5r^4)$
-2			$6xy$	$30xyz$	$30xy(7z^2 - 3r^2)$	$630xyz(3z^2 - r^2)$	$630xy(33z^4 - 18z^2r^2 + r^4)$
-3				$15y(3x^2 - y^2)$	$105yz(3x^2 - y^2)$	$105y(3x^2 - y^2)(9z^2 - r^2)$	$945zy(3x^2 - y^2)(11z^2 - 3r^2)$
-4					$420xy(x^2 - y^2)$	$3780xyz(x^2 - y^2)$	$3780xy(x^2 - y^2)(11z^2 - r^2)$
-5						$945y(5x^4 - 10x^2y^2 + y^4)$	$10395yz(5x^4 - 10x^2y^2 + y^4)$
-6							$20790xy(3x^2 - y^2)(x^2 - 3y^2)$

which are equivalent to the recurrence relation (Gradshteyn and Ryzhik, 1994, eq. 8.733.2) for associated Legendre functions and, together with

$$\Theta_n^m = (2n-1) \frac{x+iy}{r^2} \Theta_{n-1}^{m-1} \quad \text{and} \quad Y_n^m = \frac{x+iy}{2n} Y_{n-1}^{m-1} \quad (54)$$

as well as their counterparts for $m = -n$, allow for an efficient and stable evaluation of $\Theta_n^m(\mathbf{r})$ and $Y_n^m(\mathbf{r})$.

Differentiating these relations with respect to time, one obtains recursion relations for the time derivatives of the harmonic functions. For example,

$$(n^2 - m^2) \dot{Y}_n^m = (2n-1) [\dot{z} Y_{n-1}^m + z \dot{Y}_{n-1}^m] - 2\mathbf{r} \cdot \dot{\mathbf{r}} Y_{n-2}^m - r^2 \dot{Y}_{n-2}^m. \quad (55)$$

Alternatively, from equations (50) and (51) one may also directly derive

$$\dot{\Theta}_n^m = \dot{\xi} \Theta_{n+1}^{m+1} - \dot{z} \Theta_{n+1}^m + \dot{\eta} \Theta_{n+1}^{m-1}, \quad \text{and} \quad (56)$$

$$\dot{Y}_n^m = \dot{\xi} Y_{n-1}^{m+1} + \dot{z} Y_{n-1}^m + \dot{\eta} Y_{n-1}^{m-1}. \quad (57)$$

A.5.2 Real-valued spherical harmonics

Because of the anti-symmetry relation (39), the complex spherical harmonics defined above are redundant: there are only $2n+1$ independent (real) harmonics per order, in agreement with the counting in Section A.1. Hence, for any practical application one needs an appropriately reduced set of $2n+1$ real-valued independent spherical harmonics per order. The simplest option is to consider real and imaginary parts of the complex-valued harmonics with $m \geq 0$:

$$U_n^m \equiv \begin{cases} \Im(Y_n^{|m|}) = \frac{1}{2i}(Y_n^{-m} - Y_n^{-m*}) & m < 0, \\ \Re(Y_n^{|m|}) = \frac{1}{2}(Y_n^m + Y_n^{m*}) & m \geq 0; \end{cases} \quad (58a)$$

and

$$T_n^m \equiv \begin{cases} \Im(\Theta_n^{|m|}) = \frac{1}{2i}(\Theta_n^{-m} - \Theta_n^{-m*}) & m < 0, \\ \Re(\Theta_n^{|m|}) = \frac{1}{2}(\Theta_n^m + \Theta_n^{m*}) & m \geq 0. \end{cases} \quad (58b)$$

The relevant relations for these real-valued spherical harmonics are best directly transcribed from the corresponding complex relations.

A.6 Accelerating FMM relations

The FMM kernels M2L, M2M, and L2L (equations 3b,d,e) all require $\mathcal{O}(p^4)$ operations. However, if the interactions or translations are along the z -axis, the costs are only $\mathcal{O}(p^3)$ because $Y_n^m(\hat{\mathbf{z}}) = \delta_{m0}/n!$.

One method to exploit this is to first translate along the z -axis and then perpendicular to the z -axis. For a vector \mathbf{r}_\perp perpendicular to the z -axis, $Y_n^m(\mathbf{r}_\perp)$ vanishes whenever $n+m$ is even. This implies that a translation along \mathbf{r}_\perp can be done faster than a general translation (in the limit of $p \rightarrow \infty$, twice as fast).

This splitting method cannot be applied to the M2L kernel (3b) (because it is not a translation), which occurs many more times in the FMM algorithm than the M2M and L2L kernels. To accelerate the M2L kernel, one can exploit that a rotation only costs $\mathcal{O}(p^3)$ operations, too. Thus, if one first rotates into a frame in which the interaction is along the z axis, applies the M2L kernel in the rotated frame, and finally rotates back into the original frame, the total costs are still $\mathcal{O}(p^3)$.

A.6.1 Fast rotations

Since the spherical harmonics are homogeneous, a rotation (as opposed to a translation) does not mix between different orders n , and consequently the operation count is $\mathcal{O}(p^3)$. Thus, a general rotation is of the form

$$Y_n^m(\tilde{\mathbf{r}}) = \sum_{l=-n}^n \Gamma_n^{ml} Y_n^l(\mathbf{r}), \quad (59)$$

where $\tilde{\mathbf{r}}$ denotes the vector \mathbf{r} in the rotated frame. Unfortunately, the matrices Γ_n , also known as Wigner functions, are generally dense and non-trivial functions of the Euler angles. However, a rotation by angle α around the z axis is simple:

$$Y_n^m(\tilde{\mathbf{r}}) = e^{-im\alpha} Y_n^m(\mathbf{r}) \quad (60)$$

with an operation count of only $\mathcal{O}(p^2)$. With this one can build a general rotation by first rotating around the z -axis, then swapping z and x , rotating again about the z -axis (the x -axis of the original frame), swapping z and x again, and performing a final rotation around the z -axis. Like rotations, swapping coordinate axes does not mix between different orders n and can be represented as

$$\Theta_n^m(\tilde{\mathbf{r}}) = \sum_{l=-n}^n B_n^{ml} \Theta_n^l(\mathbf{r}), \quad (61)$$

where now $\tilde{\mathbf{r}}$ denotes the vector \mathbf{r} in the frame obtained by swapping two Cartesian coordinates. The important difference between equations (59) and (61) is that the matrices B_n are *constants*. Recursive relations for these swap matrices can be derived via the operator algebra of Section A.3. For example, for swapping x and z , one finds

$$2\tilde{\Delta}_1^0 = \Delta_1^1 - \Delta_1^{-1} \quad \text{and} \quad 2\tilde{\Delta}_1^{\pm 1} = \Delta_1^1 + \Delta_1^{-1} \pm 2\Delta_1^0, \quad (62)$$

